AD NUMBER

AD814787

NEW LIMITATION CHANGE

TO

Approved for public release, distribution unlimited

FROM

Distribution authorized to U.S. Gov't. agencies and their contractors; Administrative/Operational Use; May 1967. Other requests shall be referred to Air Force Weapons Lab., Kirtland AFB, NM 87117.

AUTHORITY

AFWL ltr, 30 Nov 1971

AD814787

STRESS RELAXATION IN
THE SHOCK COMPRESSION OF SOLIDS

Gordon D. Anderson   Roy C. Alverson
William J. Murri   Sathyanarayana V. Hanagud

Stanford Research Institute
333 Ravenswood Avenue
Menlo Park, California 94025
Contract AF 29(601)-7119

TECHNICAL REPORT NO. AFWL-TR-67-24

May 1967

AIR FORCE WEAPONS LABORATORY
Research and Technology Division
Air Force Systems Command
Kirtland Air Force Base
New Mexico

Research and Technology Division
AIR FORCE WEAPONS LABORATORY
Air Force Systems Command
Kirtland Air Force Base
New Mexico

PAGES NOT FILMED ARE BLANK

STRESS RELAXATION IN THE SHOCK COMPRESSION OF SOLIDS

Gordon D. Anderson   Roy C. Alverson
William J. Murri   Sathyanarayana V. Hanagud

Stanford Research Institute
333 Ravenswood Avenue
Menlo Park, California 94025
Contract AF 29(601)-7119

TECHNICAL REPORT NO. AFWL-TR-67-24

FOREWORD

This technical report has been reviewed and is approved.

JOSEPH B. WEBSTER III
Captain, USAF
Project Officer

EDGAR M. MUNYON
Colonel, USAF
Chief, Physics Branch

CLAUDE K. STAMBAUGH
Colonel, USAF
Chief, Research Division

ABSTRACT

(Distribution Limitation Statement No. 2)

The purpose of the work reported here was to investigate nonsteady-state behavior
in the early stages of one-dimensional shock propagation. This behavior has been
termed stress relaxation. The work consisted of an experimental phase and a
theoretical-computational phase. In the experimental phase, stress-time profiles
resulting from impact by a gas-gun projectile were observed in hard and soft 2024
aluminum and in polyethylene at various distances from the plane of impact.
Quartz gages were used for the measurements in aluminum, and manganin wire gages
were used in polyethylene. Peak stress amplitudes were about 14 kbar in aluminum;
there was a pronounced decay in amplitude of elastic precursor with propagation
distance. The peak stress in polyethylene was varied from 3 to 11 kbar; non-
steady-state effects were also observed, although no elastic wave was evident.
In the theoretical and computational phase, several mathematical models of stress
relaxation were developed. Computations based on these models have been performed
by the method of characteristics and by the artificial viscosity method of von
Neumann and Richtmyer. It has been found that the two-parameter model of stress
relaxation predicts the experimental results more closely than does the one-
parameter model. During this investigation, it was found that no artificial
viscosity is needed when stress-relaxing models are used. Some preliminary
results on the inclusion of thermodynamic behavior have been obtained, and it
is shown that a consistent model can be formulated on the basis of equilibrium
thermodynamics.

CONTENTS

CONTENTS

ILLUSTRATIONS

ILLUSTRATIONS

TABLES

SECTION I

INTRODUCTION

One of the current tasks of the Air Force Weapons Laboratory (AFWL) is to achieve a physical understanding and mathematical description of shock wave propagation in solids. This is a major undertaking because of the breadth of interest in materials, pressure ranges, and time scales. Stanford Research Institute has attempted for several years to aid the Weapons Laboratory in this task by carrying out research on shock propagation, equations of state, shock measurement techniques, and structural response. The work reported here is a continuation of our effort to be responsive to the needs of AFWL. We are concerned here with the early stages of shock formation and in particular with the phenomenon of "stress relaxation." This term refers, in the present context, to a change with time of the shear yield strength of a shock-compressed material. The time dependence of the shear strength arises from the combination of the very rapid loading (strain) rate and the finite time required for the material to flow under the applied shear stress.

To describe shock wave propagation, the equations of motion must be supplemented by constitutive relations describing the physical state of the material, e.g., the stress-strain behavior. The constitutive relations in general use at present are considered to be independent of the time scale of the problem. This treatment can be only an approximation, however, because real solids require a finite time to respond to any stimulus and hence will show time-dependent properties on some time scale.

In this project all the experiments were performed using plane geometry, and the computational models were set up to describe plane wave propagation. Let us, therefore, consider the plane case in some detail. The initial shock front is produced by a very rapid acceleration of a surface of the specimen (in the x direction, say), as by impact of a projectile. If the initial acceleration is infinite then one may consider the initial compression (along ABC in Figure 1, for example) of the material to be elastic.. Because the strain must be uniaxial, i.e., the macroscopic strain is zero parallel to the shock front, and because the material can

1
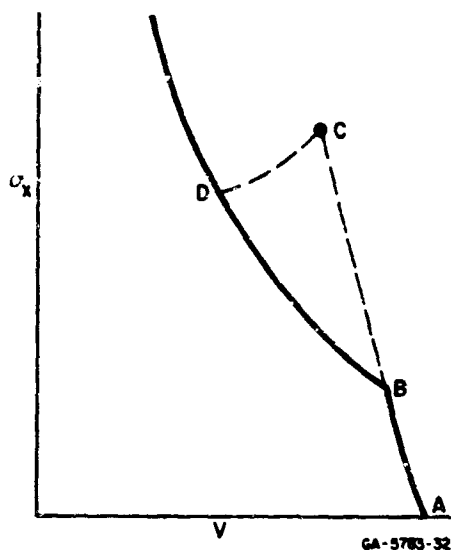
FIG. 1 ILLUSTRATION OF RELAXATION
FROM INSTANTANEOUS STRESS
(Point C) TO EQUILIBRIUM STRESS
(Point D)

...pport a shear stress, the lateral stress $\sigma_y (=\sigma_z)$ will be less than the normal stress σ_x. However, the instantaneous shear stress produced is greater than the elastic forces can support and shear yielding begins on a microscopic scale—even though macroscopic lateral strain remains zero. This yielding, requiring a finite time, allows σ_x to relax from its instantaneous value at C to an equilibrium value at D as the shear stress relaxes to its equilibrium value. The state D is now reached across two waves, the first being an elastic precursor wave of final amplitude AB (B is called the Hugoniot elastic limit), and the second having amplitude BD. During the relaxation process, the precursor amplitude will decrease with propagation distance, asymptotically approaching AB. The proximity of point D to the curve of hydrostatic compression (isothermal) depends on the magnitude of the equilibrium shear strength. If the material can support essentially zero shear stress after reaching equilibrium, point D lies on the hydrostat. The larger the equilibrium shear strength, the higher point D lies above the hydrostat. Equilibrium stresses greater than those predicted from quasi-static tensile tests are frequently observed. This phenomenon may occur because the equilibrium yield strength depends upon the hydrostatic stress. On the other hand it may be only an apparent equilibrium value because the relaxation time is long (many microseconds) compared with the duration of a shock experiment.

Section II of this report describes exploratory stress-relaxation experiments in aluminum and polyethylene. This work was done in the Poulter Laboratories of Stanford Research Institute. Section III is concerned with the development of mathematical models and techniques to describe stress relaxation. This work was performed in the Institute's Mathematics Department. Although the two phases were carried out relatively independently, the experimental phase defined the phenomena to be

2

described mathematically and also provided s ne data to be used in ap-
plying the theory that was developed.

This report builds on previous (nonsystematic) studies in these and
other laboratories; however, the problems investigated are in no sense
completely solved. Much more work will be required before time-dependent
effects in shock propagation are fully understood.

SECTION II

EXPERIMENTAL WORK

by

G. D. Anderson and W. J. Murri

1. Background

The purpose of the experimental phase of this program was to look
for nonsteady state effects in the early stages of shock propagation and
to provide data as a guide in the choice of models to be used in the
computational phase. Two materials, one metal and one plastic, which
would be expected to exhibit different types of nonsteady behavior were
chosen for study. The metal was 2024 aluminum. Since the Hugoniot
elastic limit of 2024 aluminum is known to depend upon the hardness,
both very soft and very hard samples were studied. The plastic chosen
was a highly crystalline polyethylene.

For both materials the experiments were designed to observe the
shape of an effectively infinite duration plane pressure pulse as a
function of distance from the impact face. The pulses were generated by
impact from a thick, flat projectile accelerated by a gas gun. In most
cases the projectile head was of the same material as the target sample;
a constant particle velocity boundary condition could thus be maintained
at the impact surface plane. Stress-time profiles were recorded by
quartz gages for the aluminum and by mangenin wire gages for the
polyethylene.

2. Experimental Technique

a. Aluminum

Previous work on 2024 aluminum (Ref. 1) has demonstrated an elastic
precursor amplitude varying from about 1 to 6 kbar depending upon the
initial hardness of the material. In this project we investigated
nonsteady-state elastic-plastic behavior in hard and soft aluminum. The
2024 alloy was chosen instead of pure aluminum since a much greater
difference in hardness could be obtained by heat treatment of the alloy.
Sheets of stock 2024-T351 aluminum ranging in thickness from 0.0195 to

5

0.627 inch were commercially heat treated.* The greatest hardness was attained by artificial aging for nine hours at a temperature of 375°F. The softest aluminum was attained by annealing. This process consisted of heating the material to 750°F at a rate of 50°F/hour, holding for two hours at 750°F, cooling at 50°F/hour to 450°F, and then air cooling. The hardness of the aged aluminum was Rockwell B85 and that of the annealed aluminum was Rockwell B0.

After heat treatment the specimens were cut into circular plates for mounting on target assemblies and gas gun projectile heads. Target and projectile flatness are essential for achieving simultaneous impact. Therefore all projectile heads and target plates were lapped; departure from flatness was held to less than 0.0005 inch across a 2½-inch diameter.

Quartz gages were chosen to record the stress-time profiles in aluminum because of the close impedance match of aluminum and quartz. The target assembly construction showing the sample, quartz gage, tilt pins, and epoxy support is shown schematically in Figure 2. The four tilt pins are positioned within 0.002 mm of the impact surface and record the simultaneity of impact. The epoxy support is made of "C-7" epoxy to which glass beads have been added to increase its shock impedance to match that of quartz, thereby minimizing the effect of lateral rarefactions.

A complete description of the technique of mounting and aligning the target perpendicular to the axis of the gun barrel has been given by Linde and Schmidt (Ref. 2). Aluminum projectile heads of the same material as the target were bonded onto stock aluminum projectiles with "910" cement. Care was taken to insure that the plane of the flat face of the head was perpendicular to the axis of the projectile. The projectile heads were made sufficiently thick so that no reflected wave from the back surface of the projectile head could reach the quartz gage during the time the pressure profile was being recorded.

The projectile velocity was maintained at approximately 600 ft/sec, a speed which produced a plastic wave amplitude of about 14 kbar. This choice was made so that the steady-state elastic wave amplitude would be approximately half that of the plastic wave amplitude in the hardened

---

* This work was done by the Department of Metallurgical Research, Kaiser Aluminum and Chemical Corporation, Spokane, Washington.

LOCATING HOLES FOR DOWEL PINS

PROJECTILE IMPACT AREA

TILT PIN

CONTACT WHISKER GAGE AREA

SECTION AA

0 cm 5

9C-5396-5

FREE SURFACE OF SPECIMEN

GUN BARREL

PROJECTILE

LINEAR ARRAY VELOCITY PINS

VACUUM MANIFOLD

VACUUM

"O" RING SEAL

RADIAL VELOCITY PINS (3)

ADAPTER RING

SIGNAL CABLES

QUARTZ GAGE

EPON ADHESIVE

TILT PINS (4)
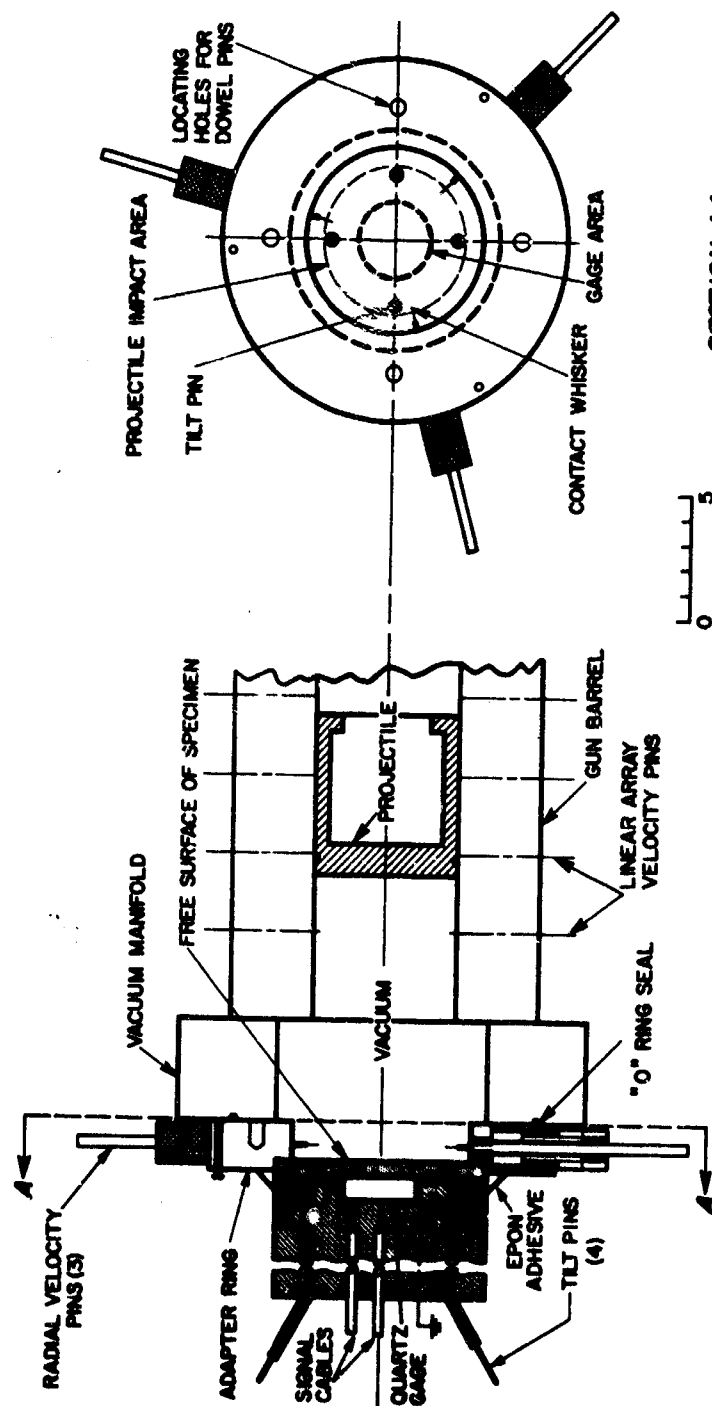
FIG. 2 CROSS-SECTION VIEW OF TARGET ASSEMBLY MOUNTED ON END OF GAS GUN

7

aluminum. In this way both waves could be conveniently observed on the same oscilloscope trace and the linear range of the quartz crystal gage would not be exceeded.

b. Polyethylene

All the polyethylene samples were cut from the same 1¼-inch thick sheet of "Hi-fax."[*] Test cores were taken at several positions in the sheet and examined for uniformity of density and crystallinity. The density as determined by volume and mass measurements was $0.938 \pm 0.002 \, gm/cm^3$. X-ray patterns were taken in three mutually perpendicular directions. The patterns indicated a degree of crystallinity greater than 90 percent and very small differences in orientation between directions. For shot construction, polyethylene samples were cut into circular disks ranging in thickness from 0.031 to 0.75 inch.

Manganin wire pressure transducers (Ref. 3) were chosen to monitor the stress profiles in the polyethylene. The reasons for this choice were that (1) the impedance mismatch between quartz and polyethylene would complicate interpretation of quartz records, and (2) manganin could be imbedded directly in polyethylene, thereby introducing a minimum perturbation on the wave profile. Manganin wire gages also occupy much less area on a specimen for a given length of recording time than do quartz gages. Because of their small size it was possible to use two wires at different depths in the target from the impact plane in each shot. This made it possible to observe the same wave front at two positions.

A shot assembly is shown in Figure 3. The usual target alignment procedure (see Ref. 2) relies upon the electrical conductivity of the target; since polyethylene is nonconductive this procedure was modified. An additional O-ring groove was cut in the adapter ring so that the target assembly could be held by vacuum seal to the adapter ring. A lapped aluminum plate was substituted for the polyethylene assembly and the adapter ring was aligned according to the procedure outlined in Ref. 2. The adapter ring was then clamped securely into position to prevent movement during venting of the gun barrel to atmospheric pressure. The flat aluminum plate was then removed and replaced with the polyethylene target assembly. Finally, the gun barrel was evacuated again.

Purchased from Cadillac Plastic Company.

8

TILT PINS

GAGE LEADS TO
POWER SUPPLY
AND SCOPES

TILT PINS (4)

POLYETHYLENE

PIECES CEMENTED
WITH EPOXY FROM
LOCTITE TEFLON
BONDING KIT.

€
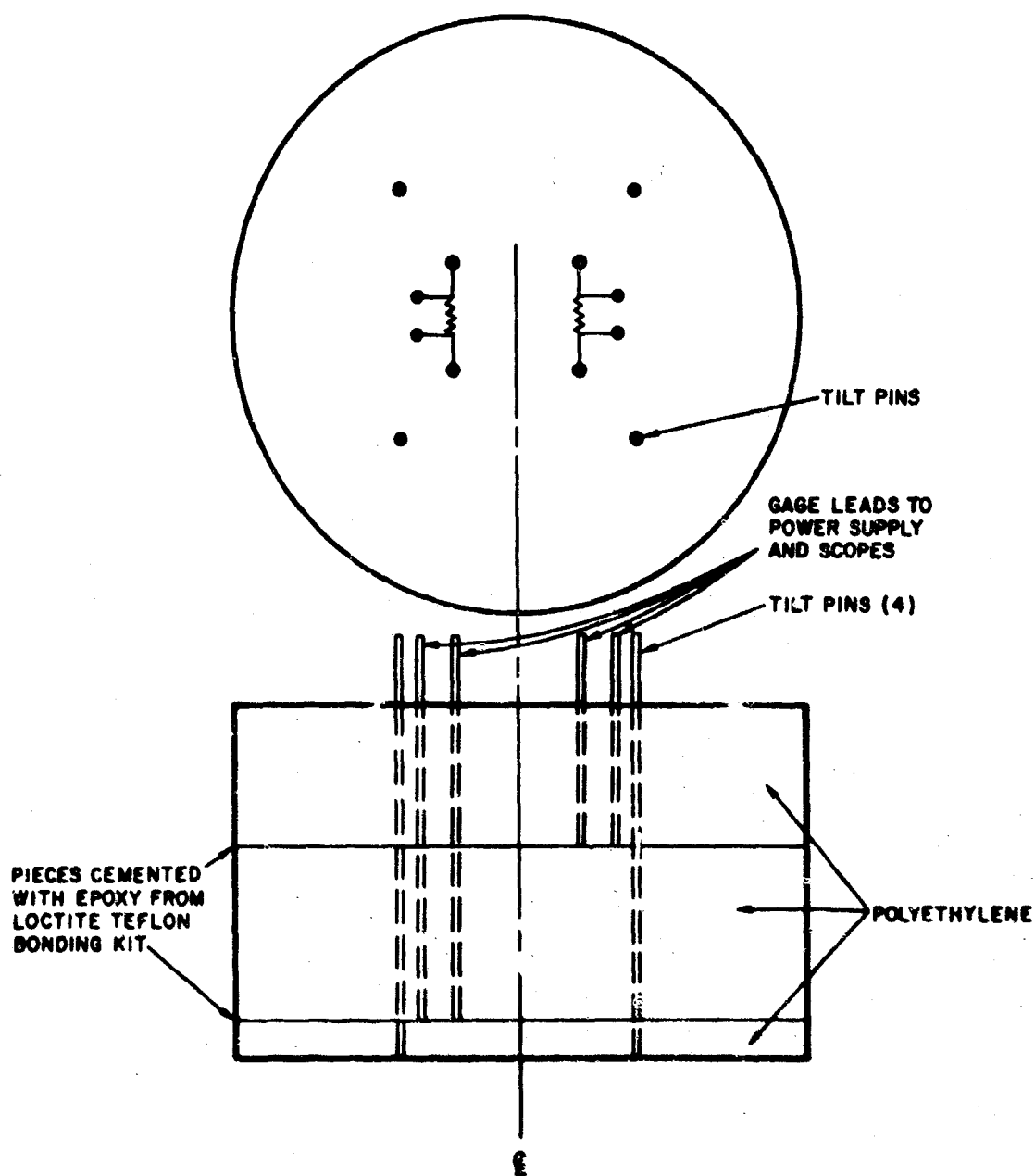
64-9703-1

FIG. 3 POLYETHYLENE TARGET DESIGN SHOWING MANGANIN GAGE CONFIGURATION

Polyethylene heads were mounted on aluminum projectiles. The polyethylene heads were 0.75 inch thick to prevent reflected waves from the aluminum backing from overtaking the initial shock during the experiment. In order to close the tilt pins upon impact it was necessary to cover the polyethylene projectile head with a thin layer (0.001 inch) of aluminum foil which was electrically connected to the projectile body and hence to ground. Flat surfaces were much more difficult to prepare on polyethylene projectile heads than they were on aluminum. Consequently both projectile tilt and nonflatness of the target contributed to nonsimultaneity of impact. The contribution to wave tilt due to projectile tilt was reduced significantly by using 12-inch long projectiles weighing approximately 2400 gm, whereas 3-inch projectiles weighing about 260 gm were used in the aluminum studies.

The peak pressures induced into most of the polyethylene targets were in the 2 to 3 kbar range, although three shots were performed at higher pressures.

c. Recording Voltage Across Manganin Wire at Low Stress Levels

The voltage change across the sensitive portion of the manganin wire for shock pressures of 2 to 3 kbar is 10 to 20 mv. It is necessary to observe this voltage variation on top of a 2v turn-on step in the sensing wire. As discussed in Ref. 3, the ratio of the change in resistance of the wire to the initial resistance of the wire is proportional to the stress.

A constant current (turned on a few microseconds prior to shock arrival) is passed through the wire during an experiment and the percentage change in voltage drop across the sensitive portion of the wire is measured. Consequer ly it is necessary to measure either the value of the current or the initial voltage across the wire (approximately 2v), and to measure the change in voltage due to the passage of the shock wave (approximately 10 to 20 mv). The pressure as a function of time can be found from the resulting oscilloscope records.

In practice certain oscilloscopes have their sensitivity adjusted to observe the entire voltage change across the wire, i.e., the 2v turn-on plus the 10-20 mv pressure signal on top of it; other oscilloscopes operating at greater sensitivity observe only the 10-20 mv pressure voltage in order to resolve the detail of the wave shape. To display the

signal due to the small pressure pulse, a negative 2v must be fed into
the oscilloscope to balance the positive 2v from the power supply. The
power supply voltage, however, is not always exactly 2v (or whatever the
predetermined value is), but may vary by a few percent depending upon
the length of time the power supply capacitors are allowed to charge.
This small variation between the power supply turn-on voltage and the
preset compensating voltage may be sufficient to cause the sweep of the
high-sensitivity oscilloscopes to be off-scale. Therefore a special cir-
cuit was designed to eliminate the need for presetting a compensating
voltage to offset the power supply voltage.

The circuit is shown schematically in Figure 4. Any signal from the
gage, such as the turn-on signal from the power supply, is sent along two
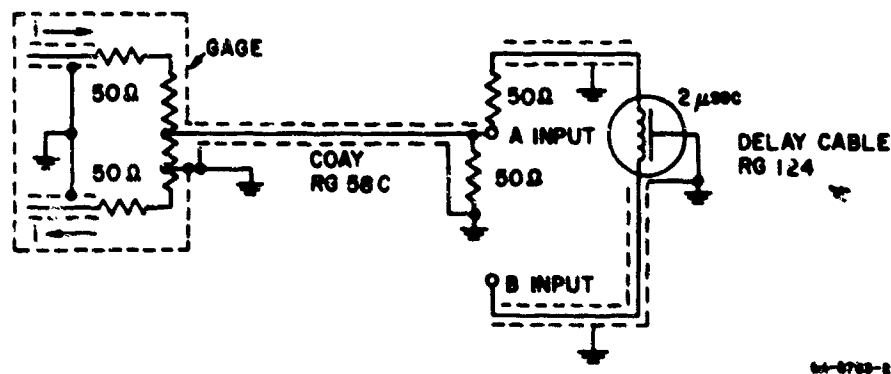
FIG. 4 TIME-DELAY REFLECTOMETER CIRCUIT

parallel paths. On one path it goes immediately to the A input of the
amplifier and on to the oscilloscope. Along the other path it is delayed
for 2 μsec and is then fed into the negative B input of the amplifier.
At 2 μsec after turn on, the circuit returns the signal reaching the os-
cilloscope to zero. Thus if the power supply is turned on at least 2 μsec
prior to the pressure signal, the turn-on voltage will be automatically
compensated for, regardless of its amplitude. The circuit then provides a
time window of 2 μsec duration for observing the pressure pulse signal be-
fore it too is cancelled. The delay time may be varied by varying the
length of cable in the delay line.

3. Experimental Results and Conclusions

Ali shots fired during the project are listed by number and objective
in Appendix 1. Shots which were of an exploratory or development nature
are not further discussed in the following presentation of data.

11

a. Aluminum

The experimental data for hardened and annealed aluminum are presented in Table I. Shock velocities computed from the time interval between the firing of the tilt pins, which denotes impact, and the appearance of a portion of the wave at the quartz gage are generally lower than the accepted steady-state values for aluminum. The discrepancies appear greater for the thinner samples. Elastic velocities are determined from the time interval between projectile impact and arrival of the first disturbance at the quartz gage. A 0.0001-inch gap between the quartz gage and the aluminum specimen resulting from a deviation in specimen flatness could produce a delay in the response of the quartz gage which would result in the observed discrepancies. The major purpose of the experiments was to observe wave shape. Had wave velocity been of primary interest different measurement techniques would have been used.

The stress wave amplitudes in the aluminum were taken to be those recorded by the quartz. No Hugoniot data in the 10 to 20 kbar range for aluminum of the type used here are available to form a basis for estimating the quartz-aluminum mismatch. Graphical interpolation of aluminum data (Ref. 1) between the Hugoniot elastic limit and about 25 kbar indicates no difference in the impedance of quartz and that of soft aluminum. The hardened aluminum is slightly higher in impedance; this could result in the quartz reading as much as 0.5 kbar lower than the true aluminum pressure at the 15 kbar level. Since the effects observed are time-dependent, the stress-particle velocity state in the aluminum does not lie on the Hugoniot. Therefore, since the impedance mismatch is very small, an attempt to correct the quartz reading using an interpolated graphical Hugoniot for aluminum when the aluminum state does not lie on that Hugoniot would not significantly enhance the value of the data.

Wave profiles in hardened aluminum as recorded by quartz gages are shown in Figure 5. The sample thicknesses varied from 3.2 to 15.7 mm. In Figure 5a, the record from a 3.2 mm sample, it can be seen that a precursor whose amplitude was nearly that of the plastic wave was forming. In Figures 5b and 5c (records from 7.89 mm and 15.75 mm samples), the precursors have separated more from the plastic wave and decreased in amplitude. The Hugoniot elastic limit for 2024-T4 is about 5.4 kbar. The aluminum studied here is considerably harder than T4, and the quartz record indicates a precursor amplitude of 7.9 kbar at a depth of 15.75 mm. It is

12

Table I

ALUMINUM SHOT DATA

SHOT NUMBER	PROJECTILE		TARGET		VELOCITY OF FIRST MOTION	ELASTIC WAVE[b]			PLASTIC WAVE[b]		
	Tilt[a] (μsec)	Velocity (mm/μsec)	Type of Aluminum	Thickness (mm)	$_0U_1$ (mm/μsec)	$_eU_{1/2}$ (mm/μsec)	$_eP_B$ (kbar)	$_eP_F$ (kbar)	$_pU_{1/2}$ (mm/μsec)	$_pP_B$ (kbar)	$_pP_F$ (kbar)
12172	0.032	0.171	Soft	3.22	5.94	–	–	–	5.39	–	12.6
12168	0.025	0.197	Soft	7.91	5.76	5.34	1.6	2.9	5.0	–	15.5
12170	0.043	0.181	Soft	7.92	6.00	–	–	–	5.45	–	13.0
12175	0.016	0.205	Soft	7.93	6.23	5.90	2.3	3.8	5.58	–	14.6
12169	0.060	0.194	Soft	15.86	6.00	5.83	1.4	2.0	~5.0	–	12.5
12807	0.014	0.197	Hard	0.475	–	–	–	–	–	–	14.0[c]
12808	0.043	0.197	Hard	0.788	–	–	–	–	–	–	14.2[d]
12173	<0.010	0.184	Hard	3.26	5.3	4.27	12.2	12.6	~3.5	–	13.1
12171	0.048	0.180	Hard	7.89	6.02	5.62	10.0	10.7	5.0	–	13.5
12174	0.015	0.202	Hard	15.85	6.29	6.10	7.1	7.9	5.41	14.6	16.1

[a] Tilt across center conductor of quartz gage (½ inch).

[b] See diagram for definition of symbols.

[c] Stress relaxed to 13.0 kbar 0.5 μsec after impact (0.31 μsec after peak stress was reached). Stress subsequently increased beyond 14.0 kbar.

[d] Stress relaxed to 13.2 kbar 0.6 μsec after impact (0.35 μsec after peak stress was reached). Stress subsequently increased beyond 14.2 kbar.
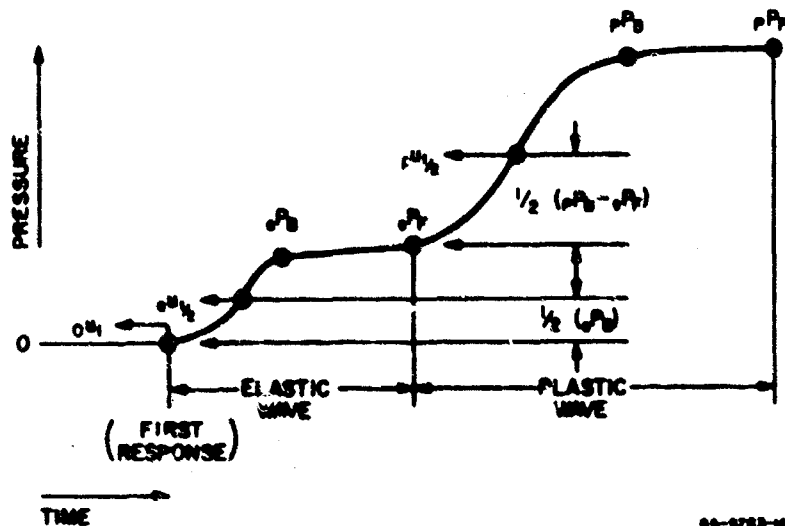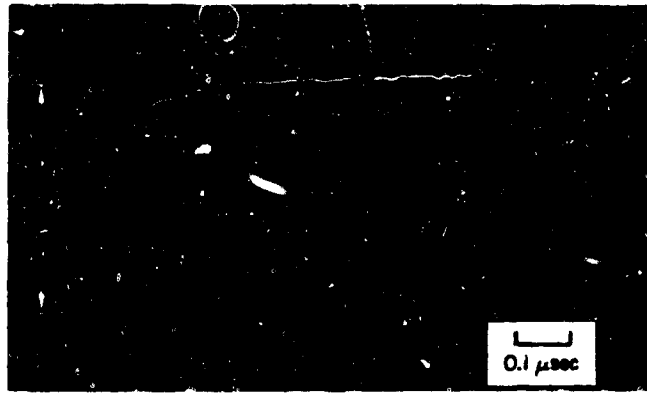
(a) SHOT 12,173 —— 3.261mm THICK
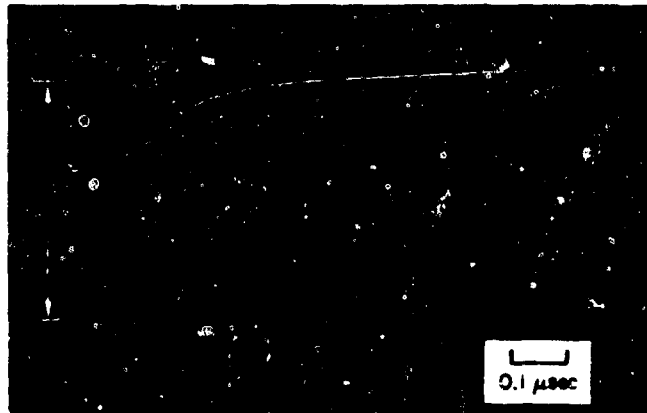
(b) SHOT 12.171 —— 7.899mm THICK
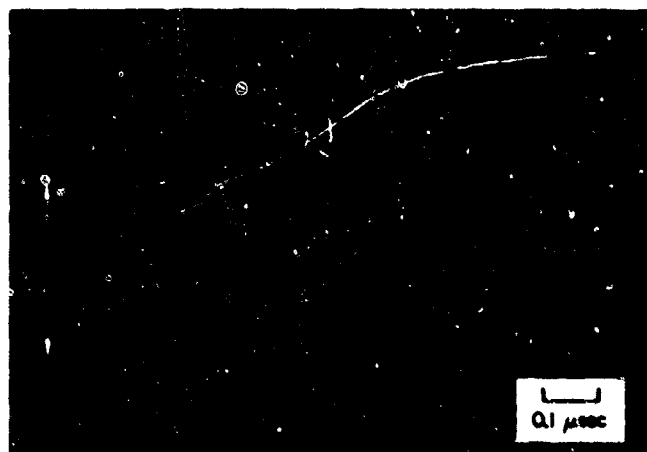
(c) SHOT 12.174 ——15.85mm THICK

FIG. 5 QUARTZ GAGE RECORDS
FOR HARDENED 2024 ALUMINUM

14

believed that at this depth the elastic wave amplitude had closely approached the Hugoniot elastic limit.

Wave profiles in soft 2024 aluminum show a different type of behavior. Quartz gage records are shown in Figure 6. As with the hard aluminum, the projectile velocity was maintained at about 600 ft/sec, inducing a plastic wave amplitude of about 14 kbar into the material. The quartz record in Figure 6a is the wave profile emerging from a 3.2 mm sample. A dip in gage voltage occurred after the initial rise to near-peak plastic wave pressure. This dip has been observed on several shots (see the elastic wave profile in Figure 5c). It is not presently being interpreted as a precursor because its duration and amplitude were always approximately the same (whereever it occurred), regardless of specimen thickness and hardness.

This dip at top of the quartz stress profile has also been seen with quartz on "Plexiglas," so it is not clear at present whether this is due to the behavior of quartz under certain circumstances or whether it is a nonsteady-state effect in the materials under consideration. Excluding the dip at the top of the record in Figure 6a, no indication of a double wave is evident. The quartz record from a 7.94 mm thick specimen is shown in Figure 6b. Here again the dip in the gage record appears near the top of the wave profile. However, a precursor is clearly evident near the bottom of the pressure rise. In Figure 6c, the quartz record shows the stress profile emerging from a 15.86 mm sample; the peak pressure is not visible but the precursor is clearly well out in advance of the plastic wave.

The wave profiles in the soft aluminum differ from those in the hard in that, when the precursor is resolvable from the plastic wave, it has almost achieved its steady-state amplitude. The precursor in the hard aluminum, however, breaks out at an amplitude only slightly less than that of the plastic wave. This implies that the relaxation of elastic stress occurs at a more rapid rate in soft annealed aluminum than it does in hardened aluminum. Relaxation of shear stress is achieved by plastic flow. It is quite reasonable to expect this flow to occur more rapidly in annealed aluminum, where the dislocations are more mobile, than in hardened aluminum where the dislocations are pinned. The decay of precursor amplitude with propagation distance is shown in Figure 7.

In a symmetrical impact of a thick projectile into a thick target of the same material, a relaxation of the plastic wave amplitude might also be expected. Consider a material, such as aluminum, which behaves

15
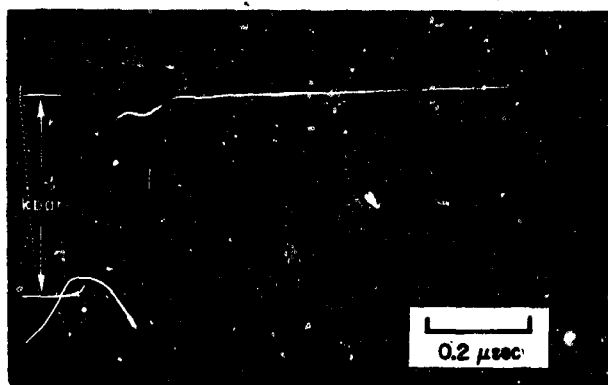
(a) SHOT 12,172 — 3.23mm THICK
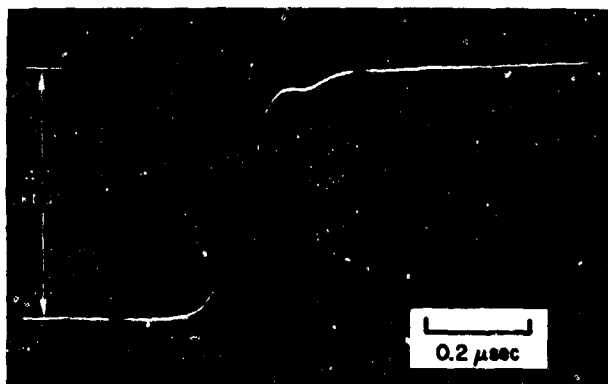
(b) SHOT 12,175 — 7.94mm THICK
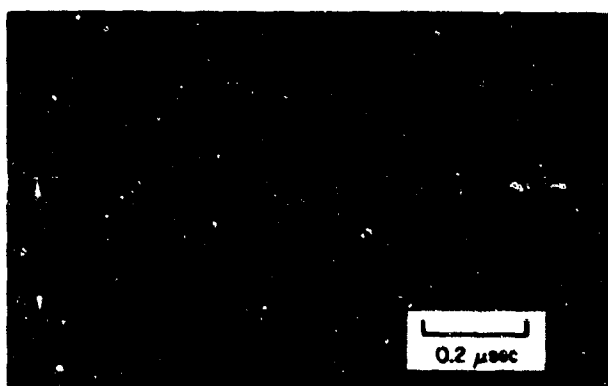
(c) SHOT 12,169 — 15.86mm THICK

FIG. 6   QUARTZ GAGE RECORDS FOR
FOR ANNEALED 2024 ALUMINUM

16
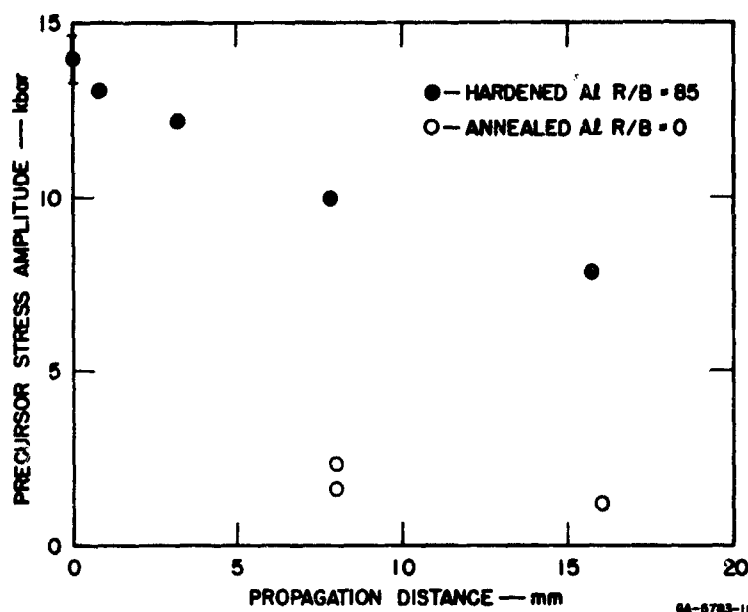
FIG. 7   DECAY OF ELASTIC PRECURSOR AMPLITUDE
WITH PROPAGATION DISTANCE IN 2024 ALUMINUM

elastically up to a certain normal stress σ_e in uniaxial strain and then
yields by plastic flow.   The stress-particle velocity Hugoniot is shown
in Figure 8 by the curve OBC, and the stress σ_e, above which the material
no longer behaves elastically under steady-state conditions, is called
the Hugoniot elastic limit.   If this material is impacted by a projectile
of the same material moving at a velocity W, the stress-particle velocity
state in the projectile when steady state is reached will be on the curve
$WB'C$.   Because of the symmetry of the impact the curves OBC and $WB'C$ are
mirror images reflected about particle velocity $W/2$.

Let us now assume that the impact is perfectly simultaneous (no tilt)
and that the response of a mass element to a step input is initially
elastic followed by a relaxation of the excess shear stress above the
yield stress to the final plastic state.   Upon impact the material at the
interface is initially shocked to state A because of its elastic response.
As relaxation of the shear stress occurs the stress decreases and reaches
C when relaxation is complete.   The relaxation of the stress at the inter-
face is communicated to the wave front, which during this relaxation time
will have propagated into the material.   The "attenuation" of peak initial
stress due to the relaxation results in some interior particle being
shocked elastically to a lower amplitude stress state, such as D.   This

17
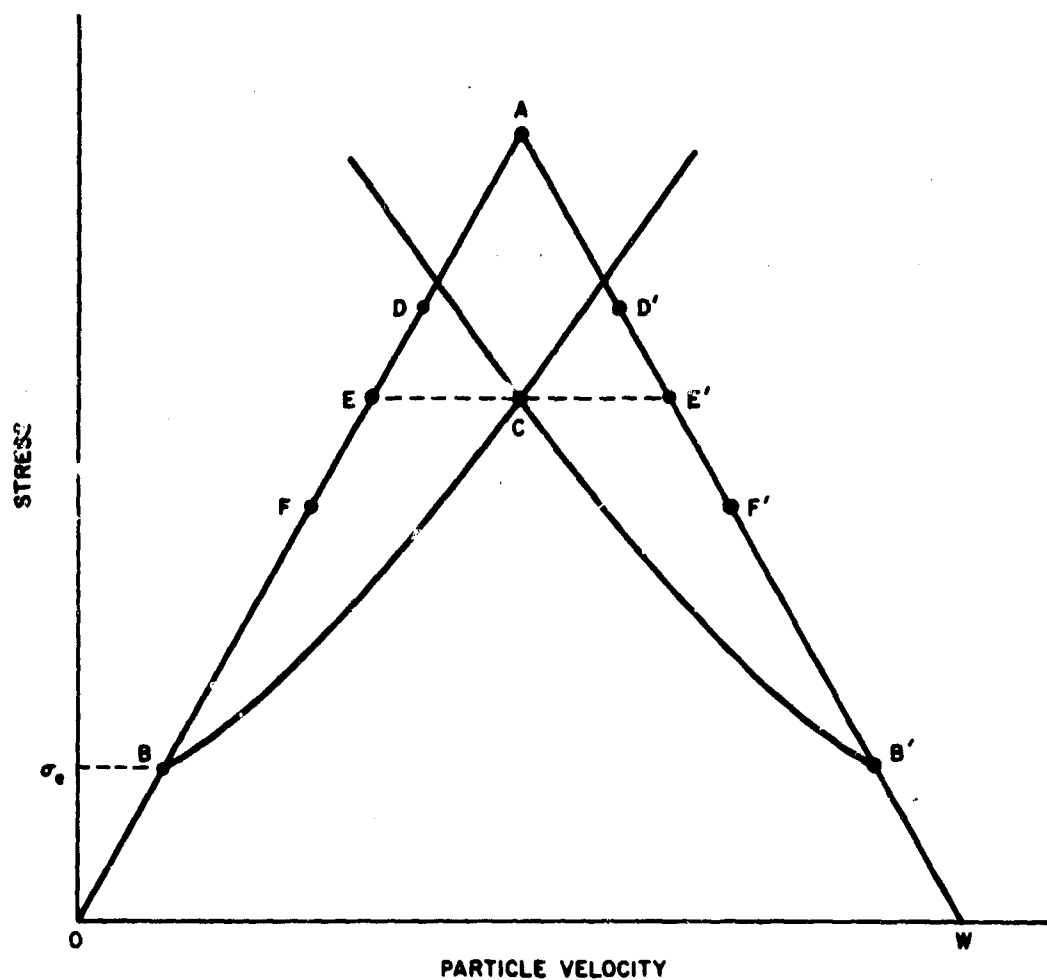
FIG. 8 PLOT OF STRESS vs PARTICLE VELOCITY SHOWING A POSSIBLE
MECHANISM FOR STRESS RELAXATION

particle then relaxes toward C along some path. All particles must ulti-
mately reach state C because of the symmetry of the impact. As yet no
double wave structure has been formed. At some point the stress at the
wave front will have been attenuated to point E, which is just the value
of the steady-state final stress. The mass element which is initially
shocked to E achieves its relaxation by accelerating at constant stress
to point C. As a result of the stress and particle velocity gradients in
the wave, some subsequent particle is shocked elastically to point F and
is then further compressed plastically to state C. It is at states below
E that the double wave structure appears. The particle that is shocked
through states OFC experiences a double wave structure. This process of

18

decay of the elastic precursor continues until point B, the Hugoniot elastic limit, is reached. Particles at greater depth experience two steady-state waves in which they are shocked elastically to B and then plastically to C.

This is just one suggested model for the process by which the wave could approach steady state. Other equally plausible models can be considered, in which the initial states lie on curves other than linear extensions of the elastic portion of the Hugoniot. However, in all models the boundary condition of constant particle velocity at the interface is required by symmetry of the impact. This means that the interface relaxes from the initial stress to point C along a path of constant particle velocity. Other particles in the target will accelerate with decreasing or increasing stress toward point C.

In the experiments no significant decrease in the plastic stress was observed. The final plastic stresses recorded were consistent with the stress predicted from existing Hugoniot data and the measured projectile velocities. An extension of the elastic portion of the Hugoniot for 2024-T4 aluminum indicates that the stress difference AC at the interface amounts to about 3 kbar at the stress level under consideration. The offset DC at some interior point in the target would be correspondingly less. The experiments indicate that the relaxation of the peak plastic wave stress from A to E has occurred in both hard and soft aluminum in less than 3.2 mm of travel.

b. Polyethylene

The experimental data for polyethylene are presented in Table II. Peak stresses in most of the shots were about 3 kbar, but some shots were fired at about 5 and 11 kbar. The depths of the manganin gages from the impact plane varied from 0.78 mm to 20.3 mm. No definite elastic precursor wave could be identified in any of the shots. Peak stresses recorded for any one shot by the two gages at different depths in the target generally agreed within the limits of experimental error.[*]

Several stress profiles are shown in Figure 9. A common feature in all the observed profiles was a rapid rise to about 80 percent of the

---

[*] The manganin gages are inherently reproducible to within 3 percent; the uncertainties in reading the polyethylene records were generally greater than that.

Table II
POLYETHYLENE DATA

SHOT NUMBER	PROJECTILE		GAGE				WAVE VELOCITY DATA[b]		
	Tilt[a] (μsec)	Velocity (mm/μsec)	No.	Depth (mm)	Stress[b] (kbar)		U_0 (mm/μsec)	$U_½$ (mm/μsec)	U_{1-2} (Between gages) (mm/μsec)
					P_P	P_F			
12511	–	0.256	–	19.1	–	2.50	~2.4	~2.38	–
12512	0.015	0.260	1 2	3.22 6.52	1.70 –	2.40 2.24	2.04 2.16	2.01 2.15	2.29
12513	0.005	0.306	1 2	6.14 12.54	– –	3.50 ~2.4	2.56 –	– –	–
12514	0.025	0.307	1 2	3.115 9.51	2.66 –	3.05 3.00	1.98 2.14	1.95 2.12	2.23
12515	0.037	0.305	1 2	3.095 6.332	2.65 2.63	3.24 3.13	2.04 2.05	2.01 2.03	2.05
12516	0.013	0.306	1 2	3.194 9.634	2.60 2.34	3.10 3.02	~2.21 ~2.33	2.60 –	
12517	0.008	0.282[c]	1 2	4.57 10.89	4.29 4.20	5.47 5.41	2.25 2.53	2.22 2.52	2.79
12804	0.022	0.298	1 2	1.20 20.15	2.40 2.95	~3.00 4.20	3.74 2.64	3.50 –	2.98
12805	0.022	0.749	1 2	1.05 20.30	– –	– 11.0	– 2.98	– 2.96	–
12806	0.011	0.722	1 2	0.787 18.15	5.0 5.7	9.9 9.8	2.77 2.82	2.58 2.81	2.82

[a] Across 6 mm, the active length of the gage.

[b] See diagram for definition of symbols.

[c] Aluminum headed projectile

$$\left(\begin{array}{c} \text{FIRST} \\ \text{RESPONSE} \end{array} \right)$$

TIME

29
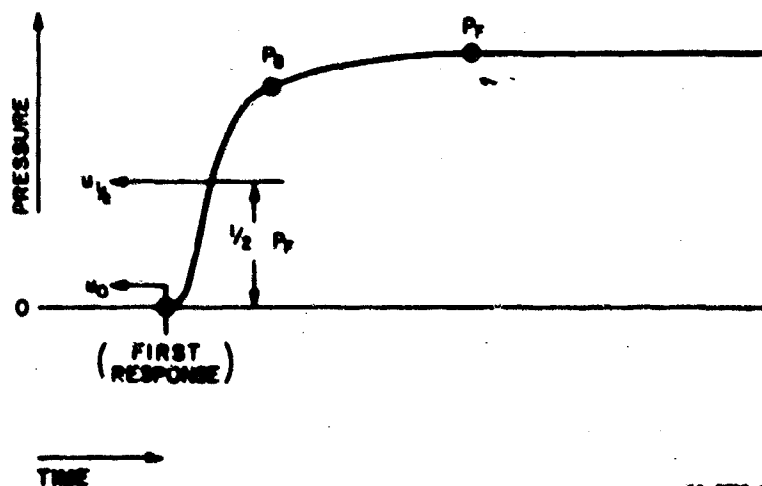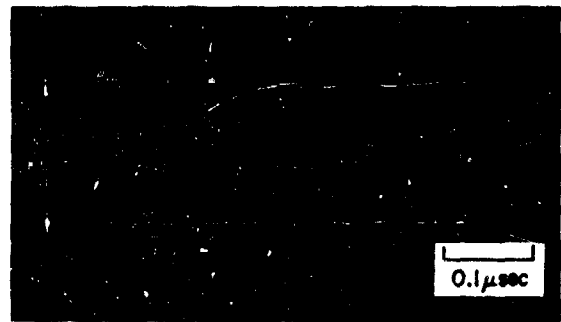
3.095mm THICK   6.332mm THICK

(a) SHOT 12,515
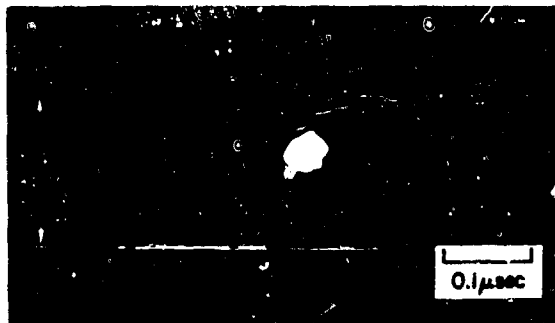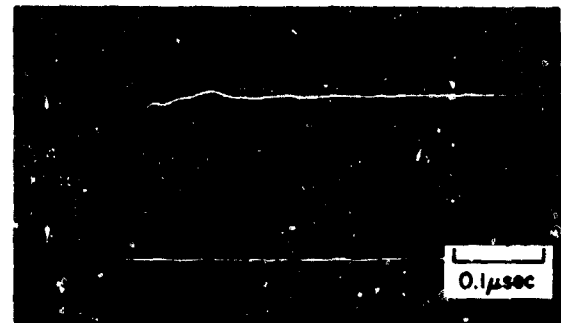
4.59mm THICK   10.89mm THICK

(b) SHOT 12,517

0.787mm THICK   18.15mm THICK

(c) SHOT 12,806

FIG. 9   MANGANIN GAGE RECORDS FOR POLYETHYLENE

final stress, followed by a much slower rise to peak stress. In Shot 12,806 (see Figure 9c) one gage was at a depth of 0.78 mm from impact and the other was at a depth of 18.1 mm. Both gages recorded the same peak stress but the deeper gage recorded a much more rounded (slower rising) pulse. The apparent double wave structure in this record is not being interpreted as an elastic plastic effect. The separation in time of the "two waves" is 0.07 μsec at 0.78 mm from impact, and only 0.11 μsec at 18.1 mm from impact. The double wave appearance was formed quite rapidly and maintained that appearance, with both waves moving at nearly the same velocity over a distance of 17.3 mm. The rounding off of the top of the wave front profile with propagation distance has also been observed in Plexiglas (Ref. 4).

The wave profiles indicate a nonsteady-state behavior, and the average shock velocities from impact to the first gage are lower in every case but one than the average shock velocity between gages. Under nonsteady-state conditions it is not strictly valid to apply the Rankine-Hugoniot jump conditions and calculate Hugoniot points. However, assuming that the wave has nearly reached steady state and that the average velocity to the final gage is quite near the instantaneous velocity, some Hugoniot points have been calculated. These data are plotted in Figure 10. Two points of Wagner, Waldorf, and Louie (Ref. 5) are included for comparison.

In a parallel program carried on simultaneously with the present work [Contract AF 29(601)-7214], similar experiments have been performed on "Teflon." A decay in peak stress of from 5 percent to 10 percent between gages was observed (gage separation about 6 mm), as well as a definite rounding of the wave front as it propagated. The wave profiles at a particular gage location were relatively flat-topped; thus the reduction of peak pressure and change of wave shape are not due to normal attenuation but are nonsteady-state effects.

It is of particular interest to compare shock velocities with measured sound velocities in polymers because of the dependence of sound velocity on frequency in certain frequency ranges, and because of the lack of evidence of an elastic precursor in any polymer yet studied. The data for polyethylene suggest that the velocity increased somewhat as the wave propagated into the specimen. This effect could result from a systematic error in measuring the impact time, although the effect was large in Shot No. 12,517 and a large timing error would be necessary to account for it. The most reliable transit times (and hence velocities) are those
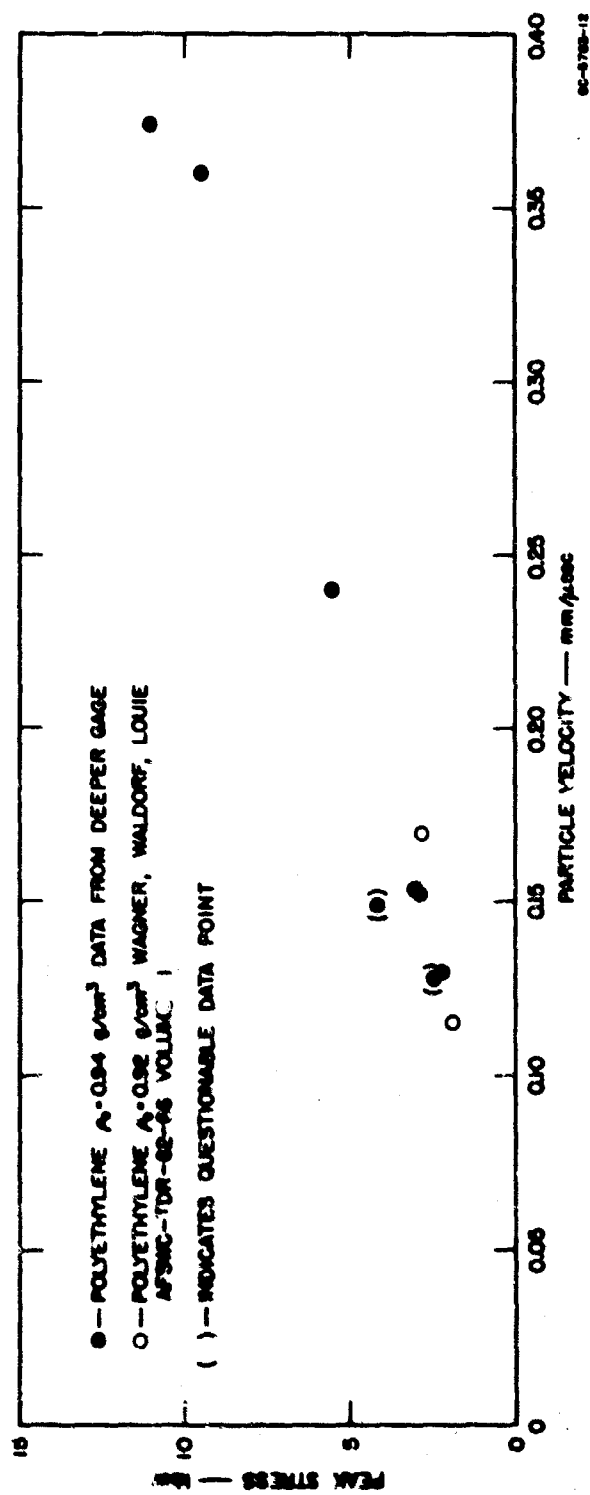
FIG. 10 POLYETHYLENE HUGONIOT

23

measured between like events—in this case, between two gage records. The corresponding shock velocity at the lowest pressure of this study (~3 kbar) is $2:2 \pm 0.1$ mm/μsec (three shots). This is to be compared with a measured (at 1 Mc/sec) longitudinal sound speed of 2.26 mm/μsec. This situation is in contrast to that for Plexiglas, in which the lowest measurements of shock velocity (~3 kbar) still exceeded measured values of the longitudinal sound velocity.

X-ray patterns were taken of some samples of polyethylene before and after impact. The patterns prior to impact indicate a high degree of crystallinity (about 90 percent) with random orientation of crystallites. Patterns taken after impact show that some of the crystallinity was lost, but there was a net orientation of the remaining crystallites such that the polymer chains tend to lie in a plane parallel to the shock front. It should be emphasized that these were not controlled recovery experiments. The specimens were subjected to gross deformations which can be avoided by proper target design.

4. Summary and Suggestions For Further Work on Stress Relaxation

The experimental effort has been directed toward the observation of stress relaxation phenomena in soft and hard 2024 aluminum and in highly crystalline polyethylene. A nonsteady-state elastic precursor which decreased in amplitude with propagation path length was clearly detected in hardened aluminum. Nonsteady-state effects were also detected in the soft aluminum and polyethylene but were not as dramatically evident as in the hardened aluminum. A low-amplitude elastic wave which did not vary by a large amount was observed in the soft aluminum. No elastic precursor was seen in the polyethylene; however, the wave shape was observed to vary as the wave propagated, indicating a nonsteady state.

The present work represents only a beginning in the much needed study of nonsteady-state propagation of low-amplitude stress waves and the mechanisms of failure of solids under rapidly applied loads. An extension of this work could profitably be directed toward studies on metals or polymers. "Stress relaxation" in the context of this project is manifested by the decay in amplitude of the elastic precursor in an elastoplastic solid as the wave propagates during the early states of shock formation, i.e., very soon after impact. This decay in amplitude is associated with the finite time required for the plastic yielding to occur. The ultimate steady-state amplitude of the elastic wave is related to the static yield

24

point of the material. Inasmuch as no elastic precursor has been observed in polyethylene (or several other polymers), it is suggested that the definition of the term "stress relaxation" be broadened to include the general process by which the wave approaches its steady-state profile.

_ a. Suggestions for Work on Metals

The present study has established the existence of stress relaxation in 2024 aluminum. The decay in amplitude of the elastic precursor with propagation distance appears greatest in hardened 2024 aluminum. Nonsteady-state behavior is visible up to a depth of at least 0.5 inch from the plane of impact. It is now clear that nonsteady-state effects are quite important, perhaps equally as important as nonhydrodynamic effects, and further investigation of these effects is required for a complete understanding of wave propagation in solids.

The present work has been devoted to observing the shape of the pressure pulse rise as a function of propagation distance. The duration of the pulses has been essentially infinite because very thick projectile heads have been used. Projectile heads have been made of the same material as the target to maintain a constant particle velocity boundary condition at the impact plane. Experiments using thin-headed projectiles should also be performed, as the long-range goal of this work is to gain a complete understanding of shock propagation. Such understanding must include the nonsteady-state behavior of the rise of the wave, the flow behind the wave, and particularly the manner in which rarefactions overtake the shock and produce attenuation. At the present time there is every reason to believe stress relaxation should affect all parts of the flow. One very important question to answer is whether stress relaxation affects the late stages of shock propagation, i.e., wave shape after a propagation distance of many initial pulse thicknesses. Also, what effect does stress relaxation have on spall thresholds and other damage criteria?

The work suggested below is aimed at continuing the efforts of the past year toward answering these questions.

(1) Aluminum. Having established stress relaxation in aluminum using very long pulses, the work must now be extended to pulses of short duration. Shock profiles should be observed after propagating several pulse widths and results should be compared to prediction of attenuation models. The effect of initial temperature on stress relaxation effects is

unknown. Experiments similar to those performed during the past year should be performed on hardened aluminum at initial temperatures from 200°C up toward melting (~660°C).

(2) <u>Other Metals.</u> Very little elastoplastic data or stress relaxation data exist for metals other than aluminum and iron. Two metals of particular interest to which the present work should be extended are tungsten and titanium. Quartz or manganin wire gages, as appropriate, should be used to observe wave shape for various thicknesses. (The manganin wire pressure gage is particularly well suited for stress propagation studies in polymers. It has already been used quite successfully in Teflon and polyethylene.) Initial conditions such as hardness and method of fabrication should also be varied as in the case of hard and soft aluminum. After investigating the behavior of long duration pulses, studies should be made of attenuation with emphasis on late stage behavior and spall prediction criteria.

Extension of the present work should first be concentrated on further studies of polyethylene. Such work should include the following:

(a) Experiments using manganin wire gages, as in the present work, should be performed at higher stress levels to determine the dependence upon stress of the nonsteady-state behavior which is observed at low stresses. These experiments should be performed on both the existing samples (for comparison with existing data) and on newly constructed samples with different microscopic structure (and hence different mechanical properties).

(b) The effect of wave rise time upon shock structure should be investigated. Foam attenuators could be used to alter the shape of the input wave. Manganin wire gages could then be used, as in the past, to look at the wave shape in the polyethylene sample resulting from different input wave shapes.

(c) The effect of initial temperature upon wave propagation is very important from both the applied and purely scientific viewpoints. Again, because of their temperature insensitivity, manganin gages are very well suited for the study of wave shapes in polyethylene at elevated temperatures.

(d) The mechanical properties of the polyethylene used in the present work appear to be affected by shocking. The material is more brittle after shocking than it was initially and X-ray patterns indicate some orientation of the crystallites which was not initially present. It is not clear at present whether the observed changes are due to the shock or to the subsequent relief by lateral rarefactions. To determine the effect of shock on the crystal structure, specially designed recovery experiments should be performed in which the strain in the sample is maintained one-dimensional as nearly as possible.

In addition, exploratory work on other plastics should be carried out to investigate the possibility of nonsteady-state effects. Carbon phenolic would be a logical candidate.

SECTION III

THEORETICAL PHASE

by

S. V. Hanagud and R. C. Alverson

1. Background

Research on shock propagation in solids has been the principal source of information leading to an understanding of the dynamic behavior and constitutive relations of these solids when subjected to very large stress and very large stress rates. In the case of metals in certain stress ranges, the wave form consists of an elastic precursor followed by a plastic shock wave which carries the material to its final stress. Some recent experimental work, (Refs. 6-9) as well as the experimental work on hard and soft aluminum done in the present research program, shows that the amplitude of the elastic wave is considerably higher than that predicted from elastic-plastic theories based on static measurements. This phenomenon can be observed if the measurements are made within the first few microseconds of the formation of the two-wave structure. As the wave propagates into the solid, the amplitude of the elastic shock wave decreases and asymptotically approaches the amplitude predicted from the usual elastic-plastic theory. The mechanism for such processes of stress relaxation (Ref. 10) depends on the particular material. The general mathematical description of wave propagation is most conveniently given in terms of Eulerian coordinates. In this coordinate system the field quantities such as displacement, velocity, density, or stresses are expressed as functions of the instantaneous position of a material particle and of the time. Using this coordinate system and making the assumption of uniaxial strain, to coincide with experimental work, the governing set of equations is:

$$\rho \dot{v} - \frac{\partial \sigma_x}{\partial x} = 0 \qquad \text{(conservation of momentum)} \qquad (1)$$

$$\frac{1}{\rho}(\dot{\rho}) + \frac{\partial v}{\partial x} = 0 \qquad \text{(conservation of mass)} \qquad (2)$$

29

$$\dot{e} \; = \; \dot{Q} + \frac{1}{\rho} p_x \dot{v} \qquad \text{(energy balance)} \tag{3}$$

and

$$f(\sigma_x, \dot{\sigma}_x, \ldots, \epsilon_x, \dot{\epsilon}_x, \ldots, e) = 0 \qquad \text{(constitutive relations)} \tag{4}$$

The symbols used in these equations are explained as follows:

$t \quad = \quad$ time

$x \quad = \quad$ Eulerian coordinate

$(\cdot) \quad = \quad$ material derivative given by $\dfrac{\partial}{\partial t} + v \dfrac{\partial}{\partial x}$

$\rho(x,t) \quad = \quad$ density

$v(x,t) \quad = \quad$ particle velocity

$\sigma_x(x,t) \quad = \quad$ normal stress in x direction (positive in tension)

$e \quad = \quad$ internal energy per unit mass

$Q \quad = \quad$ heat per unit mass added by conduction, radiative absorption, etc.

$\epsilon_x \quad = \quad$ strain in x-direction

$f \quad = \quad$ functions defining the constitutive relation, including thermodynamic variables.

The formulation of appropriate functions f based on the principles of continuum mechanics and the physical mechanism of the material is the first task. Later the solution of the set of partial differential equations with appropriate initial and boundary conditions can be used to correlate and interpret the experimental data.

In some materials, such as polyethylene, the effect of thermodynamics and viscous stresses may be more important than the stress rate effects. Then the functions f must be defined to take these into account.

2. Constitutive Relations for Stress Relaxation

The constitutive relations for stress-relaxing materials are discussed here under the assumption of uniaxial strain. Under this assumption all dependent variables are functions of one Eulerian coordinate, x, and the time. Since there is only one nonzero velocity component, the strain rates are given by

$$\dot{\epsilon}_x = \frac{\partial v}{\partial x} \tag{5}$$

and

$$\dot{\epsilon}_y = \dot{\epsilon}_z = \dot{\epsilon}_{xy} = \dot{\epsilon}_{yz} = \dot{\epsilon}_{zx} = 0 \quad .$$

The only nonvanishing components of the stress tensor are σ_x, σ_y, and σ_z, and because of symmetry under uniaxial strain we have $\sigma_y = \sigma_z$. Decomposition of the stress tensors into a hydrostatic pressure p and stress deviator D_{ij} gives

$$p = -\frac{1}{3}(\sigma_x + 2\sigma_y) \tag{6}$$

$$D_{11} = D_{xx} = \frac{2}{3}(\sigma_x - \sigma_y)$$

$$D_{22} = D_{yy} = \frac{1}{3}(-\sigma_x + \sigma_y)$$

$$D_{33} = D_{zz} = \frac{1}{3}(-\sigma_x + \sigma_y)$$

$$D_{12} = D_{21} = D_{23} = D_{32} = D_{13} = D_{31} = 0 \tag{7}$$

The formulation of the constitutive relation consists of determining the relation between p, D_{ij}, and the kinematic variables. It will be assumed that the hydrostatic pressure p is a function of density alone, i.e.,

$$p = f(\rho) \quad . \tag{8}$$

31

The function $f(\rho)$ depends on the particular material. Two suitable forms of $f(\rho)$ are

$$p = a_1\left(\frac{\rho}{\rho_0} - 1\right) + a_2\left(\frac{\rho}{\rho_\cdot} - 1\right)^2 + \ldots$$

$$p = b_1\left(1 - \frac{\rho_0}{\rho}\right) + b_2\left(1 - \frac{\rho_0}{\rho}\right)^2 + \ldots$$

When the function $f(\rho)$ is specified the remaining task is to specify the relationship between the stress deviator and the kinematic variables.

a. Elastic-Plastic Model

The very commonly used relation between the stress deviator and the kinematic variables is the familiar elastic-plastic relation. This can be described as follows. In the case of uniaxial strain there is only one independent component of the stress deviator because

$$D_{xx} = -2D_{yy} = -2D_{zz} = \frac{2}{3}(\sigma_x - \sigma_y) \quad . \tag{9}$$

In a similar way the components of the strain deviator E_{ij} are

$$E_{xx} = \frac{2}{3}(\epsilon_x)$$

$$E_{yy} = -\frac{1}{3}(\epsilon_x)$$

$$E_{zz} = -\frac{1}{3}(\epsilon_x) \quad . \tag{10}$$

The strain-rate deviators are

32

$$\dot{E}_{xx} = \frac{2}{3}\dot{\epsilon}_x = \frac{2}{3}\frac{\partial v}{\partial x}$$

$$\dot{E}_{yy} = -\frac{1}{3}\dot{\epsilon}_x = -\frac{1}{3}\frac{\partial v}{\partial x}$$

$$\dot{E}_{zz} = -\frac{1}{3}\dot{\epsilon}_x = -\frac{1}{3}\frac{\partial v}{\partial x} \quad . \tag{11}$$

If the solid is deforming elastically, i.e., if

$$|D_{xx}| \leq y, \quad y \geq 0 \tag{12}$$

then

$$D_{xx} = 2GE_{xx} \quad . \tag{13}$$

In Eqs. (12) and (13), y is the deviatoric yield stress* and G is the modulus of rigidity. Furthermore, Tresca type of yielding has been assumed. The solid is said to be deforming plastically in regions where

$$|D_{xx}| = y \quad . \tag{14}$$

Once $|D_{xx}|$ has attained the yielding value of y, $|D_{xx}|$ cannot increase beyond this value. However, the strain deviator can continue to increase.

b. Elastic-Plastic Relaxing Model

The elastic-plastic model cannot account for certain experimental observations in shock wave propagation. Measurements made within the first few microseconds have shown that the two-wave structure predicted by the elastic-plastic model is not formed instantaneously but is only realized after some time by a process of relaxation. During the relaxation process, the amplitude of the elastic wave (or elastic precursor) is considerably higher than that predicted from the elastic-plastic model. As the wave propagates into the solid the amplitude of the wave decreases and asymptotically approaches a value corresponding to the static yield stress.

_____

* $y = 2/3\gamma$ where γ is the yield stress in simple tension.

33

(1) Macroscopic Relaxation Equations

The elastic-plastic stress-strain relationships outlined above are macroscopic. They can be generalized to include stress relaxation. A simple model can be constructed by considering the rate type of the constitutive relation in the form

$$\hat{D} = F(D, \dot{E}, p) \tag{15}$$

where $\dot{E}$ is the rate of deformation tensor. The symbol $\wedge$ represents the Janmann or co-rotational type of stress rate (Ref. 11). In the case of uniaxial strain these stress rates reduce to the usual time derivatives along particle paths.

A specific relaxing type of stress-strain relationship as applied to the case of uniaxial strain can be written as

$$\dot{E}_{xx} = \frac{D_{xx} - \theta_y}{2GT} + \frac{\dot{D}_{xx}}{2G} \tag{16}$$

if

$$|D_{xx}| > y \tag{17}$$

otherwise

$$\dot{E}_{xx} = \frac{\dot{D}_{xx}}{2G} . \tag{18}$$

In these equations θ can take the value of ± 1. This accounts for the fact that yielding can take place when the absolute value of the deviator reaches y. T can be called the relaxation constant and has the dimension of time.

The first term on the righthand side of Eq. (16) takes care of the fact that the components of the stress deviator can have values greater than the static deviatoric yield stress. This then can result in the amplitude of the elastic precursor wave being much larger than the equilibrium value. The form of the term suggests that the deviator relaxes with time towards the static yield value. The second term on the righthand side of Eq. (16) takes care of the elastic deformation. This equation can be written as

34

$$\dot{D}_{xx} = \frac{\theta y}{T} + 2G\dot{E}_{xx} - \frac{D_{xx}}{T} \tag{19}$$

with the condition that

$$\dot{D}_{xx} = 2G\dot{E}_{xx} \tag{20}$$

when

$$|D_{xx}| = y \quad . \tag{21}$$

Alternatively it can be stated that when $\dot{E}_{xx} = 0$ and $D_{xx} = \theta y$; then

$$\dot{D}_{xx} = 0 \quad . \tag{22}$$

If Eq. (19) is expressed as

$$\dot{D}_{xx} = \overline{F}(D_{xx}, \dot{E}_{xx}, \rho) \tag{23}$$

we have

$$\overline{F}(\theta y, 0, \rho) = 0 \quad .$$

In a similar way

$$\dot{D}_{yy} = \overline{F}(D_{yy}, \dot{E}_{yy}, \rho) \tag{24}$$

$$\dot{D}_{zz} = \overline{F}(D_{zz}, \dot{E}_{zz}, \rho) \tag{25}$$

However, these equations will be identical to Eq. (19) in case of uniaxial strain; y may be a function of some invariants of the stress tensor in the general tensorial constitutive equation.

Further generalizations can be made by considering general forms of functions $\overline{F}$ in Eq. (19). However, these generalizations should be based on the physical mechanisms and experimental observations.

In the case of hard and soft aluminum, experimental observation indicates that a two-wave structure is formed a very short time after impact. However, the amplitude of the elastic precursor is initially very

35

large compared with the value predicted by the elastic-plastic model.
The elastic wave amplitude decreases within a few microseconds to the
steady-state amplitude of the elastic precursor as predicted by the
elastic-plastic theory. This behavior indicates that the yield stress
is very large at early times, relaxing to the static value in a few
microseconds. (This can be called the yield relaxation time.) It also
indicates that the relaxation of the elastic precursor towards the equi-
librium value is taking place much faster than the yield relaxation time
and thus is setting up the two-wave structure at a very early time. A
model to explain this behavior can be obtained by adding to Eq. (16) an
additional equation,

$$\dot{y} = \frac{y - y_0}{T_1} \qquad y > y_0 \qquad (26)$$

In this case y is no longer a constant but

$$y = y(\sigma_x, \sigma_y, \rho)$$

and decreases with time towards the static-yield value

$$y = y_0$$

Another way of generalizing the relaxation equation is as
follows. Equation (16) and Eq. (8) can be simplified by substituting in
them the expressions for p and D_{xx} in terms of σ_x, and eliminating σ_y
between the two equations. Then we have

$$\dot{\sigma}_x + F(\rho)\dot{\rho} = -F'(\rho,\sigma_x) \qquad (27)$$

where

$$F(\rho) = \frac{4G}{3\rho} + \frac{df}{d\rho}$$

and

$$F'(\rho,\sigma_x) = \frac{f(\rho)}{T} + \frac{\sigma_x}{T} - \frac{\theta y_0}{T}$$

Alternatively one can think of Eq. (27) as a one-dimensional relaxation equation with

$$F(\rho) = -\frac{d\sigma_x}{d\rho} = c^2$$

the quantity c^2 is the square of the sound speed and $F'(\rho, \sigma_x)$ is the dissipation function. Then in any one-dimensional problem a function $\sigma_x = -F(\rho)$ and $F'(\rho, \sigma_x)$ should be specified. $\sigma_x = -F(\rho)$ will be the elastic σ_x, ρ relationship. This can be found from many steady-state experimental results. A function for $F'(\rho, \sigma_x)$ based on Zener's model is

$$F'(\rho, \sigma_x) = \frac{p_x - p_i}{T}, \qquad p_x = -\sigma_x ,$$

where p_i is the amplitude of elastic precursor when complete relaxation has taken place. This would be the amplitude of the elastic precursor on the basis of elastic-plastic models. Another form for $F'(\rho, \sigma_x)$ can be

$$F'(\rho, \sigma_x) = \frac{p_x - p_i(\sigma_x, \rho)}{T_1}$$

and

$$\dot{p}_i = -\frac{p_i - \bar{p}}{T_2} \tag{28}$$

where T_2 is the relaxation constant for the yield stress.

The value of p_i on any particle is of significance from the time the particle comes under the influence of the leading elastic shock wave. If this time is specified as t_s and the pressure at this instance is p_s, then

$$p_i(t_s) = \bar{f}(p_s)$$

This equation specifies the initial condition for Eq. (28). A similar reasoning can be used to specify the initial condition for Eq. (26). Calculation of wave profile with these equations will be discussed later.

37

(2) Microscopic Relaxation Equations (Dislocation Mechanism)

Shear yielding and resultant plastic flow in metals are due to the motion of dislocations. A sufficient number of mobile dislocations is necessary to cause yielding. In dynamic problems a finite time is necessary for dislocation production and movement and hence for production of plastic flow. This finite time is then the cause of the large initial amplitudes of elastic precursor waves.

It is known that a sufficiently strong external stress can cause a dislocation to unpin itself and hence become mobile. Dislocations can also be created by the Frank-Read mechanism, a kind of multiplication or breeding process, and again the effective agency is stress. Once unpinned, a dislocation is free to move and contribute to yielding or plastic strain, until it again becomes trapped at another grain boundary or impurity. The total number of moving dislocations effectively contributing to the plastic strain rate at any moment is the net result of competition between the processes of unpinning or creation (sources) and of trapping (sinks).

It is natural to suppose that unpinning is an excitation process with a rate depending on the excess of shear stress over yield stress, while the Frank-Read mechanism produces new dislocations from existing ones at a rate that is proportional to the number of existing ones and that also depends on the excess shear stress. To simplify the analysis we approximate the excitation process by taking the rate simply proportional to the excess shear stress. The rate of trapping is of course proportional to the number of dislocations present. These relationships can be put in mathematical form in the following way. Suppose that at some particular time the mobile dislocation density is N_a and the total dislocation density is N_t; hence, the density of pinned dislocations is $(N_t - N_a)$. Assume that the pinned dislocations become Frank-Read sources, so that a term $g_1 Z(N_t - N_a)$ contributes to dN_a/dt. The constant g_1 represents the strength of the Frank-Read source and Z is defined to be $(\tau - Y/2)$, the excess shear stress above the yield point.[*] The pinned dislocations may also become mobile by various freeing mechanisms and this contributes another term, $g_2 Z(N_t - N_a)$, to the rate dN_a/dt. We assume further that mobile dislocations can become pinned by interaction

---

[*] $Y = 3/2\, y, \quad \tau = 1/2(\sigma_x - \sigma_y); \text{ hence } Z = 3/4(\sigma_{xx} - y).$

with impurities, etc., thus contributing a rate term of the foꞁm
$-(1/T_1)N_{\blacksquare}(v/v_{\blacksquare})$, where v is the dislocation velocity and $v_{\blacksquare}$ its maximum
value. Mobile dislocations can also simply disappear irreversibly by
migration to free surfaces and voids, giving a similar term $-(1/T_2)N_{\blacksquare}(v/v_{\blacksquare})$.
These assumptions result in the following expressions for the rate of
change of the mobile and total dislocation densities:

$$\frac{dN_{\blacksquare}}{dt} = \frac{4}{3}gZ(N_t - N_{\blacksquare}) - \left(\frac{1}{T_1} + \frac{1}{T_2}\right)N_{\blacksquare}\left(\frac{v}{v_{\blacksquare}}\right) \quad ,$$

$$\frac{dN_t}{dt} = \frac{4}{3}gZ\epsilon(N_t - N_{\blacksquare}) - \left(\frac{1}{T_2}\right)N_{\blacksquare}\left(\frac{v}{v_{\blacksquare}}\right) \quad . \tag{29}$$

Here $g = (3/4)(g_1 + g_2)$, and $\epsilon = g_1/(g_1 + g_2)$. It can be seen from the
definition that ϵ is a number between zero and unity. When ϵ is close to
zero, a pinned dislocation is more likely to become freed than to create
a new dislocation. A value of ϵ close to unity means that a pinned dis-
location will probably create a new one rather than become freed. If the
stress history at some point in the solid is known, Eq. (29) can be
integrated to give the total and mobile dislocation densities at this
point.

In order to get some idea of the choice of parameters in this
model, we consider the application of a constant stress. The ratio
$(v/v_{\blacksquare})$ will then be constant, since the dislocation velocity is assumed
to be a function of the stress alone. Eliminating N_t from Eq. (29) gives

$$\frac{d^2N_{\blacksquare}}{dt^2} + \left[(1-\epsilon)\frac{4}{3}gZ + \left(\frac{v}{v_{\blacksquare}}\right)\left(\frac{1}{T_1} + \frac{1}{T_2}\right)\right]\frac{dN_{\blacksquare}}{dt}$$

$$+ \frac{4}{3}gZ\left(\frac{v}{v_{\blacksquare}}\right)\left[\frac{(1-\epsilon)}{T_2} - \frac{\epsilon}{T_1}\right]N_{\blacksquare} = 0 \quad .$$

We want the mobile dislocation density to increase with the application
of stress. To ensure this, the equation above must have a solution
which increases with time. This requires that

$$\frac{(1 - \epsilon)}{T_2} - \frac{\epsilon}{T_1} < 0 \qquad .$$

This condition will be satisfied if we choose ϵ close to unity and $T_2 > T_1$.

The dislocation velocity is assumed to depend on the applied shear stress. Following Gilman and Johnston (Ref. 12).

$$v = v_{\blacksquare} \exp \left[- \frac{B}{\tau - \frac{y}{2}} \right]$$

where

τ = shear stress = $\frac{1}{2} (\sigma_x - \sigma_y)$

$\frac{1}{2} y$ = shear stress at which plastic flow starts

$v_{\blacksquare}$ = maximum dislocation velocity

B = a constant.

Now the shear strain rate is given by

$$\dot{\gamma} = bvN_{\blacksquare}$$

where b is the Burger's vector. The remaining task is to interpret $\dot{\gamma}$ in terms of $\dot{\epsilon}_x$.

Under the conditions of uniaxial strain

$$\epsilon_y = \epsilon_z = 0$$

Furthermore, the total strain can be split into elastic and plastic strains. Then

$$\epsilon_x = \epsilon_x^e + \epsilon_x^p$$

$$\epsilon_y = \epsilon_y^e + \epsilon_y^p$$

$$\epsilon_z = \epsilon_z^e + \epsilon_z^p$$

Because of symmetry.

$$\epsilon_y^e = \epsilon_z^e$$

$$\epsilon_y^p = \epsilon_z^p$$

Furthermore

$$\epsilon_y^e + \epsilon_y^p = 0 \quad .$$

If it is assumed that the plastic strain does not contribute to any volume change

$$\epsilon_x^p + 2\epsilon_y^p = 0$$

Then

$$\epsilon_y^p = -\frac{\epsilon_x^p}{2} \quad .$$

Under uniaxial strain the maximum shear strain is oriented at $45°$ to the x axis and the maximum plastic shear strain rate is given by

$$\dot{\gamma} = \frac{1}{2}(\dot{\epsilon}_x^p - \dot{\epsilon}_y^p)$$

Then

$$\dot{\gamma} = \frac{3}{4}\dot{\epsilon}_x^p \quad .$$

The relaxation function is

$$F = 2G\dot{\epsilon}_x^p = \frac{8}{3}Gb_v N_{\blacksquare} \tag{30}$$

where b is the Burger's vector and $N_{\blacksquare}$ must be calculated from Eq. (29).

41

c. Thermodynamic Considerations

The results of many wave calculations are in disagreement with experiment. There are many reasons for these discrepancies, one of which is undoubtedly the fact that the calculations are based on constitutive relations which are independent of time; i.e., stress relaxation and viscous effects are neglected. However, in some materials the macroscopic properties may be highly temperature-dependent, and theoretical predictions should therefore be based on thermodynamic as well as purely mechanical considerations. Most theories of wave propagation in solids are based on a governing set of differential equations which is independent of energy considerations. It is the purpose in this section to show how a theory which includes thermodynamic considerations may be constructed for a stress-relaxing solid. We consider the perfectly elastic, perfectly plastic, and the plastic stress-relaxing solids, in that order.

If we let T, S, and E denote the temperature, entropy, and internal energy per unit mass, respectively, we have from the first and second laws of thermodynamics

$$TdS = dE - \sigma_{ij}d\epsilon_{ij}$$

where σ_{ij} are the stress components and ϵ_{ij} are the strain components and we assume the summation convention over the repeated subscripts: $\sigma_{ij}\epsilon_{ij} \equiv \sigma_{xx}\epsilon_{xx} + \sigma_{xy}\epsilon_{xy} + $ etc. The relation above can be rewritten in the form

$$\left(\frac{\partial E}{\partial \epsilon_{ij}}\right)_T - \sigma_{ij} = -T\left(\frac{\partial \sigma_{ij}}{\partial T}\right)_{\epsilon_{ij}}$$

The constitutive relations considered in the present work for purely elastic behavior in the case of uniaxial strain are

$$\frac{\sigma_x + 2\sigma_y}{3} = -f(\rho)$$

and

$$\frac{\sigma_x - \sigma_y}{2G} = \epsilon_x$$

42

These equations can be solved for σ_x and σ_y in turn and the results can be substituted into the thermodynamic relation above. It is thus readily seen that if σ_x and σ_y are independent of T, that is, if G and $f(\rho)$ are independent of temperature, then

$$\frac{\partial \sigma_x}{\partial T} = \frac{\partial \sigma_y}{\partial T} = 0$$

and

$$\frac{\partial E}{\partial \epsilon_{ij}} - \sigma_{ij} = 0$$

This equation can be integrated directly to give the internal energy, once the strains are given. Thus the purely elastic model which is mechanically consistent does not violate either the first or the second law of thermodynamics. If, in the constitutive relations given above, either or both G and f depend upon the temperature, we then append to this system of equations the equation which expresses conservation of energy:

$$\frac{dQ}{dt} = \rho \frac{dE}{dt} - \frac{1}{2} \sigma_{ij} \dot{\epsilon}_{ij} \quad .$$

In this equation Q is the heat flux or heat input. This equation, together with the constitutive relations and the equations governing **conservation of mass and momentum and the first and second laws of** thermodynamics then give a consistent set of equations with which theoretical studies of wave propagation in a perfectly elastic heat-conducting medium can be made.

We now consider the perfectly plastic solid for simplicity, and use the *von Mises* yield criterion

$$\epsilon_{ij} = \mu D_{ij} , \quad D_{ij} D_{ij} = 2k^2$$

where ϵ_{ij} is the strain rate and D_{ij} is the stress devictor. By simple manipulation of the above we have

$$\mu = \frac{\sqrt{\dot{\epsilon}_{ij} \dot{\epsilon}_{ij}}}{k} \quad .$$

43

We also assume here for simplicity that the material is incompressible. The equation of heat conduction or conservation of energy then becomes

$$\frac{dQ}{dt} = \frac{dE}{dt} - k\sqrt{\dot{\epsilon}_{ij}\dot{\epsilon}_{ij}}$$

Again, if the yield stress is independent of temperature the mechanical problem is separate from the thermal problem and the latter may be solved after the mechanical problem has been solved.

The case of a stress relaxing elastic-plastic medium is much more complex but a combination of the procedures given in the two cases above applies. The system of equations which is both thermodynamically and mechanically consistent is given by the conservation laws (mass, momentum, and energy), the constitutive relations, and the combined expressions for the first and second laws of thermodynamics. If the material properties are independent of the temperature the problems are separate, but if $f(\rho)$ and/or the relaxation constants depend on the temperature, then the heat conduction problem must be solved simultaneously with the mechanical problem.

These considerations have been based on the ideas of equilibrium thermodynamics, and to date no computations have been attempted using the theory discussed above. For simple cases such computations are entirely feasible if sufficient data on the temperature dependence of the constitutive relations are known. Further extension of this work to nonequilibrium thermodynamics depends on formulating a definition of entropy which is consistent with the equilibrium case. The thermodynamic considerations are likely to be important in some materials, since high temperatures may be obtained at impact surfaces and the resulting temperature distribution may then alter the wave shape and may be a source of high energy dissipation.

44

3. Method of Computation

a. Characteristics of the Differential Equations

The equations governing the wave propagation under uniaxial strain can be written in the following way.

Equation expressing conservation of mass:

$$\frac{\partial \rho}{\partial t} + v \frac{\partial \rho}{\partial x} + \rho \frac{\partial v}{\partial x} = 0 \tag{31}$$

Newton's law:

$$\frac{\partial \sigma_x}{\partial x} - \rho \left(\frac{\partial v}{\partial t} + v \frac{\partial v}{\partial x} \right) = 0 \quad . \tag{32}$$

In these equations x is the Eulerian coordinate, σ_x is the stress in the x-direction, v is the particle velocity in the x-direction, and ρ is the density. Equations (31) and (32), together with the appropriate constitutive relationships, complete the governing equations.

Constitutive relations:

$$-p = \left(\frac{\sigma_x + 2\sigma_y}{3} \right) = -f(\rho) \tag{33}$$

$$\frac{\dot{D}_{xx}}{2G} + \frac{D_{xx} - \theta y}{2GT} = \dot{E}_{xx} \quad . \tag{34}$$

In these equations the dots represent the derivative along the particle paths. Furthermore, Eq. (34) assumes the simple one-parameter macroscopic model for the stress relaxation. This equation will be simplified and put in a form such that it can be generalized to include other models.

By using the following relationship

$$D_{xx} = \frac{2}{3} (\sigma_x - \sigma_y)$$

Equation (34) becomes

$$\frac{\dot{\sigma}_x - \dot{\sigma}_y}{2G} + \frac{\sigma_x - \sigma_y - \theta \bar{y}}{2GT} = \dot{\epsilon}_x \tag{35}$$

45

where

$$\bar{y} = \frac{3}{2} y \quad . \tag{36}$$

By definition

$$\dot{\epsilon}_x = \frac{\partial v}{\partial x} \quad .$$

Then from Eq. (31)

$$\dot{\epsilon}_x = -\frac{\dot{\rho}}{\rho} = \frac{1}{\rho} \left(\frac{\partial \rho}{\partial t} + v \frac{\partial \rho}{\partial x} \right) \quad . \tag{37}$$

Equation (35) now becomes

$$\dot{\sigma}_x - \dot{\sigma}_y + \frac{1}{T} (\sigma_x - \sigma_y - \theta\bar{y}) = -2G \frac{\dot{\rho}}{\rho} \quad . \tag{38}$$

This equation and Eq. (33) can be used to eliminate σ_y. Then the following equation is obtained;

$$\dot{\sigma}_x = -\left(\frac{4G}{3\rho} + \frac{df}{d\rho} \right) \dot{\rho} - \frac{f(\rho)}{T} - \left(\frac{\sigma_x}{T} - \frac{\theta\bar{y}}{T} \frac{2}{3} \right) \tag{39}$$

or

$$\dot{\sigma}_x + c^2 \dot{\rho} = -F'(\rho, \sigma_x) \tag{40}$$

where

$$c^2 = \frac{4G}{3\rho} + \frac{df}{d\rho} = F(\rho) \tag{41}$$

$$F' = \frac{f(\rho)}{T} + \frac{\sigma_x}{T} - \frac{\theta\bar{y}}{T} \frac{2}{3} \quad . \tag{42}$$

Equation (40) is in a form in which most of the constitutive relationships involving stress relaxation and only the first-time derivative of stress can be written. Equation (40) can also be written as

$$d\sigma_x = -F(\rho)d\rho - F'(\rho, \sigma_x)dt \quad . \tag{43}$$

Then

$$\frac{d\rho}{dt} = -\frac{F'(\rho, \sigma_x)}{f(\rho)} - \frac{d\sigma_x}{dt} \frac{1}{F(\rho)} \quad . \tag{44}$$

The equation expressing the conservation of mass can now be rewritten as

$$\frac{d\sigma_x}{dt} + F'(\rho,\sigma_x) = \rho F(\rho) \frac{\partial v}{\partial x} \quad . \tag{45}$$

By introducing the notation

$$p_x = -\sigma_x \tag{46}$$

equation (45) becomes

$$\frac{dp_x}{dt} + F'(\rho,\sigma_x) = \rho F(\rho) \frac{\partial v}{\partial x} \quad . \tag{47}$$

The use of the definition of the derivative along the particle path yields

$$\frac{\partial p_x}{\partial t} + v \frac{\partial p_x}{\partial x} + \rho c^2 \frac{\partial v}{\partial x} = F'(\rho,p_x) \quad . \tag{48}$$

The equation of motion [Eq. (32)] can also be written as

$$c \left\{ \frac{\partial p_x}{\partial x} + \rho v \frac{\partial v}{\partial x} + \rho \frac{\partial v}{\partial t} \right\} = 0 \quad . \tag{49}$$

By adding Eqs. (48) and (49) we have

$$\frac{\partial p_x}{\partial t} + (v + c) \frac{\partial p_x}{\partial x} + \rho c \left\{ \frac{\partial v}{\partial t} + (v + c) \frac{\partial v}{\partial x} \right\} = F' \quad . \tag{50}$$

Similarly, by subtracting Eq. (49) from Eq. (48)

$$\frac{\partial p_x}{\partial t} + (v - c) \frac{dp_x}{dx} - \rho c \left\{ \frac{\partial v}{\partial t} + (v - c) \frac{\partial v}{\partial x} \right\} = F' \tag{51}$$

The form of Eqs. (50) and (51) suggests that they can be written as

$$\left(\frac{dp_x}{dt} \right)_a + \rho c \left(\frac{dv}{dt} \right)_a = F'(\rho,p_x) \tag{52}$$

47

and

$$\left(\frac{dp_x}{dt}\right)_\beta - \rho c \left(\frac{dv}{dt}\right)_\beta = F'(\rho, p_x) \quad . \tag{53}$$

where

$$\left(\frac{d}{dt}\right)_\alpha \quad \text{and} \quad \left(\frac{d}{dt}\right)_\beta$$

represent the total derivatives along the paths α and β defined by

$$\alpha: \quad \frac{dx}{dt} = v + c \tag{54}$$

and

$$\beta: \quad \frac{dx}{dt} = v - c \quad . \tag{55}$$

The paths α and β define the characteristics (Ref. 13) of the set of equations governing the problem and Eqs. (52) and (53) are the two compatibility relations valid along each of these characteristics. These equations can be used to set up a scheme of numerical integration of the initial-boundary value problem.

These equations are valid only if $|D_{xx}| \geq y$. If $|D_{xx}| \leq y$, the material is in the elastic regime. Equations (54) and (55) for the characteristics are still valid; however, the compatibility relations are

$$\left(\frac{dp_x}{dt}\right)_\alpha + \rho c \left(\frac{dv}{dt}\right)_\alpha = 0$$

and

$$\left(\frac{dp_x}{dt}\right)_\beta + \rho c \left(\frac{dv}{dt}\right)_\beta = 0 \quad .$$

An alternate way of deriving the equations of characteristics and the compatibility relations based on the existence proof of Cauchy-Kowalewski is explained in Appendix II.

48

b. Numerical Method

The mesh points are taken to be fixed. The fixed interval Δx is along the x-axis, and Δt along the time axis. The ratio $\Delta x/\Delta t$ is determined from a knowledge of the maximum values of particle velocity and the sound speed c. The set of fixed mesh points is shown in Figure 11. The curve labeled I represents the interior boundary and the curve labeled II represents the leading shock wave penetrating into the undisturbed medium.
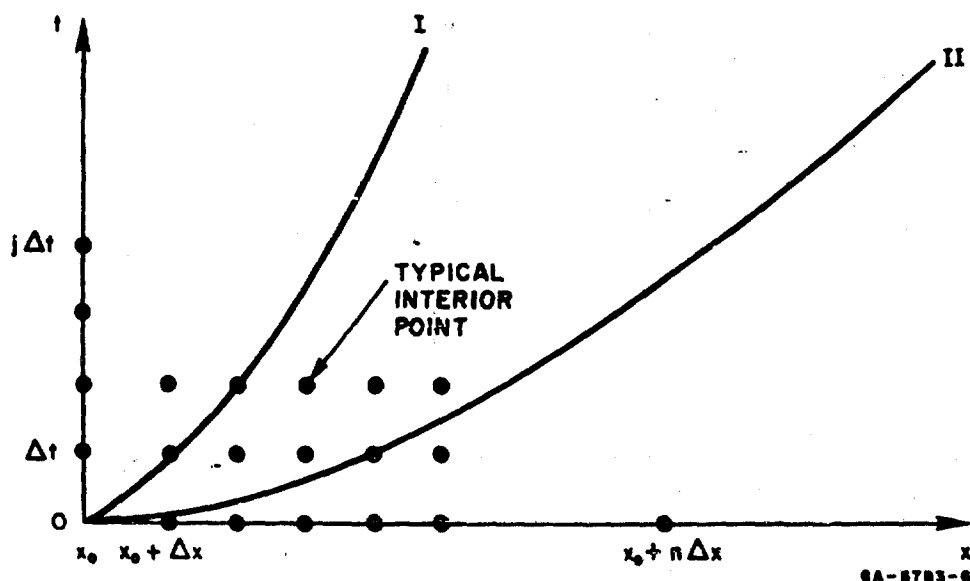
FIG. 11 FINITE DIFFERENCE MESH FOR THE METHOD OF CHARACTERISTICS

The numerical determination of the field quantities at a mesh point $x = x_0 + n\Delta x$, $t = j\Delta t$ differs according to whether the point is on either Curve I or II or on an interior point, in Figure 11.

(1) Numerical Determination at a General Interior Point

In Figure 12, it is assumed that the point labeled x lies somewhere on a horizontal line $t = t_1$, and that the points x_1, x_2, and x_3 are on a horizontal line $t = t_1 - \Delta t$; the x coordinates of x_2 and x_3 are $x_1 - \Delta x$ and $x_1 + \Delta x$, respectively.

It is also assumed that the values of p_x, ρ, and v are known at points x_1, x_2, and x_3. x_2 must lie either on or to the right of Curve I of Figure 11 and x_3 must lie either on or to the left of Curve II. The values of the field quantities at x are to be determined.

49

The first step is to approximate the characteristic curves through x by straight lines and find their intersections with the horizontal line $t = t_1 - \Delta t$. To this end we approximate the curve with slope $dx/dt = v^*$ by the straight line through x with slope

$$\frac{dx}{dt} = \frac{v(x_1) + v(x_2)}{2} \quad . \tag{56}$$
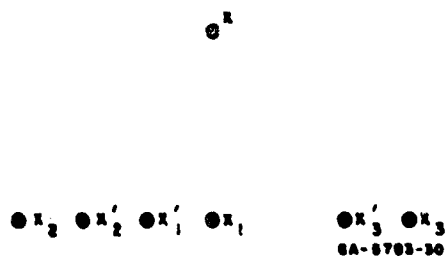
FIG. 12 TYPICAL MESH POINT FOR A GENERAL INTERIOR POINT

This curve represents the particle path along which Eq. (40) is valid.

The intersection of this line with $t = t_1 - \Delta t$ is then denoted by x_1' in Figure 12. The x coordinate of x_1' is then readily computed through the formula

$$x_1' = \frac{[v(x_1) + v(x_2)]}{2} \Delta t + x_1 \quad . \tag{57}$$

From Eq. (57) we note that x_1' may be greater than, equal to, or less than x_1, according to whether

$$\frac{v(x_1) + v(x_2)}{2} \gtrless 0 \quad .$$

If $x_1' \leq x_1$ we define

$$\lambda_1 = \frac{x_1' - x_2}{\Delta x} \tag{58}$$

and

$$\lambda_1 = \frac{x_1' - x_1}{\Delta x} \tag{59}$$

if

$$x_1' > x_1 \quad .$$

___

* The curve $dx/dt = v$ represents the characteristic curve along which the constitutive relations are valid (see Appendices II and III).

The values of p_x, ρ, and v at x_1' are then found by interpolation through the formula

$$F(x_1') = F(A) + \lambda_1 [F(B) - F(A)] \qquad (60)$$

where F is successively equal to p_x, ρ, or v, and A is x_1, B is x_2 if λ_1 is given by Eq. (58), and A is x_1 and B is x_3 if λ_1 is given by Eq. (59).

In a similar manner points x_2' and x_3' of Figure 11 are found as the intersections of the straight lines which approximate the curves

$$\frac{dx}{dt} = v \pm c$$

with

$$t = t_1 - \Delta t \quad .$$

Thus

$$x_2' = \frac{[(v + c)(x_1) + (v + c)(x_2)]}{2} \Delta t + x_1 \qquad (61)$$

and

$$x_3' = \frac{[(v - c)(x_1) + (v - c)(x_3)]}{2} \Delta t + x_1 \quad . \qquad (62)$$

In the equation above, $(v + c)(x_1)$, etc. denote the value of $(v + c)$ at point x_1. It is to be noted that x_2' lies between x_2 and x_1, and x_3' lies between x_1 and x_3 because of the way in which the ratio $\Delta x/\Delta t$ was taken. We then define

$$\lambda_2 = \frac{x_2' - x_2}{\Delta x} \qquad (63)$$

and

$$\lambda_3 = \frac{x_3' - x_1}{\Delta x} \qquad (64)$$

and the values of p_x, ρ, and v at x_2' and x_3' are then given by Eq. (60).

$$F(x_1') = F(A) + \lambda_1 [F(B) - F(A)]$$

where x_1' is successively x_2' and x_3', etc.

The finite difference equations which must be solved to give the values of p_x, ρ, and v at x can be written in the following way.

$$p_x(x) - p_x(x_2') + \rho(x_2')c(x_2')[v(x) - v(x_2')] = F'(x_2')\Delta t \qquad (65)$$

$$p_x(x) - p_x(x_3') - \rho(x_3')c(x_3')[v(x) - v(x_3')] = F'(x_3')\Delta t \qquad . \qquad (66)$$

In these equations

$$F'(x_2') = F'[\rho(x_2'),p_x(x_2')]$$

$$F'(x_3') = F'[\rho(x_3'),p_x(x_3')]$$

$$p_x(x) - p_x(x_1') = -F(x_1')[\rho(x) - \rho(x_1')] - F'(x_1')\Delta T \qquad . \qquad (67)$$

First $p_x(x)$, $v(x)$, and $\rho(x)$ are computed from these equations with $F' = 0$. Then D_{xx} is calculated from the following equation

$$D_{xx} = \frac{4G}{3} \log \frac{\rho(x)}{\rho_0} \qquad . \qquad (68)$$

If

$$|D_{xx}| < \frac{2}{3}\,\bar{y} \qquad (69)$$

the calculations are complete. If

$$|D_{xx}| \geq \frac{2}{3}\,\bar{y} \qquad (70)$$

Eqs. (65) to (67) are used to compute $p_x(x)$, $v(x)$, and $\rho(x)$ with F' in all the equations. In these calculations the value of θ is +1 if $D_{xx} \geq 0$, and $\theta = -1$ if $D_{xx} < 0$.

(2) Numerical Determination at a Point on the Boundary

In this case the point x lies on Curve I and is not necessarily one of the *a priori* fixed mesh points. Referring to Figure 13, the values of the field quantities are known at x_1, x_3, x_4, and they must be
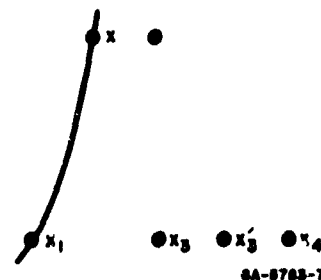
FIG. 13 TYPICAL POINT ON THE INTERIOR BOUNDARY

52

determined at x. Note that x_1 and x need not be mesh points in the fixed mesh but are both points on Curve ' nd hence on a particle path. The point x is then found from

$$x = v(x_1)\Delta t + x_1 \qquad (71)$$

where it has again been assumed that point x lies on $t = t_1$ and points x_1, x_3, x_4 lie on $t = t_1 - \Delta t$.

The point x_3' is then located by

$$x_3' = -\frac{[(v - c)(x_1) + (v - c)(x_3)]}{2} + x \quad . \qquad (72)$$

Two cases can arise in Eq. (72):

$$x_3' \leq x_3 \qquad (73)$$

and

$$x_3' > x_3 \quad . \qquad (74)$$

If Eq. (73) is satisfied, then

$$\lambda_3 = \frac{x_3' - x_1}{x_3 - x_1} \qquad (75)$$

and if Eq. (74) is satisfied

$$\lambda_{\bar{\circ}} = \frac{x_3' - x_3}{\Delta x} \quad . \qquad (76)$$

In either case, the values of the field quantities at x_3' are found by making the proper but obvious substitutions in Eq. (60).

The finite difference equations which must be solved to yield the field quantities are then:

$$p_x(x) - p_x(x_3') - \rho(x_3')c(x_3')[v(x) - v(x_3')] = F'(x_3')\Delta t \qquad (77)$$

$$p_x(x) - p_x(x_1) = -F(x_1)[\rho(x) - \rho(x_1)] - F'(x_1)\Delta t \quad . \qquad (78)$$

53

Along Curve I, $p_x(x)$ or $v(x)$ is known. Then Eqs. (77) and (78) can be used to determine the remaining two of the three quantities $p_x(x)$, $v(x)$, $\rho(x)$. Again, the quantities are computed with $F' = 0$. The stress deviator D_{xx} is computed from Eq. (78). Then if

$$|D_{xx}| < \frac{2}{3}\,\bar{y}$$

the calculations are complete. Otherwise, the calculations are done using Eqs. (77) and (78) with F'. Again $\theta = +1$ if $D_{xx} > 0$ and $\theta = -1$ if $D_{xx} < 0$.

(3) Numerical Determination at a Point on the Shock Wave

We now consider the point x to be on the shock wave as shown in Figure 14 In this instance the points x and x_1 lie on the shock wave and are not in general fixed mesh points. The coordinate of x is given by
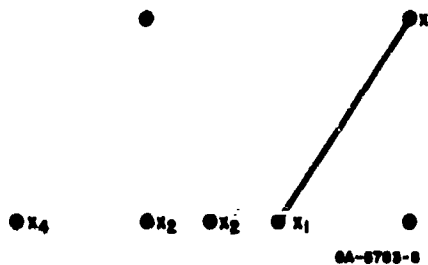
FIG. 14 TYPICAL POINT ON THE SHOCK WAVE

$$x = U(x_1)\Delta t + x_1 \quad . \quad (79)$$

where $U(x_1)$ is the shock wave velocity at x_1. The coordinate of x_2' is given by

$$x_2' = -\frac{[(v + c)(x_2) + (v + c)(x_1)]}{2}\,\Delta t + x \quad . \quad (80)$$

Again in Eq. (80) two cases can arise: If $x_2' \geq x_2$

$$\lambda_2 = \frac{x_2' - x_2}{x_1 - x_2}$$

and if $x_2' < x_2$

$$\lambda_2 = \frac{x_2' - x_4}{\Delta x} \quad .$$

54

The values of the field quantities at x_2' are found by application of Eq. (60). The field quantities at x are then determined by the equations

$$\rho_0 U(x) = \rho(x)[U(x) - v(x)] \quad (81)$$

$$p_x(x) = \rho_0 U(x) v(x) \quad (82)$$

$$p_x(x) - p_x(x_2') + \rho(x_2') c(x_2')[v(x) - v(x_2')] = F'(x_1')\Delta t \quad (83)$$

$$p_x(x) = + \frac{4G}{3} \log \frac{\rho(x)}{\rho_0} + f(\rho) \quad . \quad (84)$$

These equations are reduced to a single equation in ρ and the resulting equation is solved by Newton's method of iteration.

(4) Numerical Determination at Interior Points Near the Boundary

In this case points x_1 and x_3 will lie between Curve I and the shock wave, but point x_2 will lie outside of the region where the field quantities are to be determined.

In this case x_1' and x_3', together with the field quantities at x_1' and x_3', are determined by the same formulas as for the general interior point, but the method differs for determining x_2' and the values of the field quantities at x_2'.

If x_2' as computed from

$$x_2' = \frac{[(v + c)(x_0) + (v + c)(x_1)]}{2} \Delta t + x \quad (85)$$

is greater than or equal to x_0, the whole computation proceeds as for the general interior point, with the exception that

$$\lambda_2 = \frac{x_2' - x_0}{x_1 - x_0} \quad .$$

55

If x_2' is less than x_0, we calculate t_2' by the formula

$$t_2' = \frac{\left\{\dfrac{(v + c)(x_0) + (v + c)(x_1)}{2}\right\} t(x) - v(x_0) t(x_0) + x_0 - x_1}{\dfrac{(v + c)(x_0) + (v + c)(x_1)}{2} - v(x_0)}. \quad (86)$$

In this case

$$\lambda_2 = \frac{t_2' - t(x_0)}{\Delta t} \quad ,$$

and the values of the field quantities at t_2, shown in Figure 15, are found by using Eq. (60) with the point at x_0 for A, and $\bar{x}$ for B.
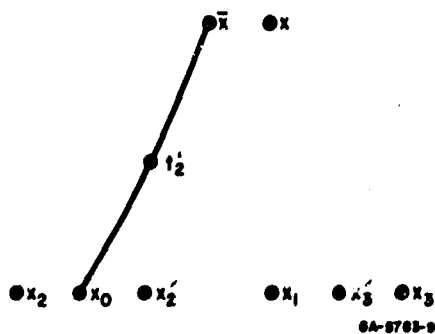
FIG. 15 INTERIOR POINT
NEAR THE BOUNDARY

The finite difference equations for determining the field quantities at x are then given by Eqs. (65) through (68) together with Eqs. (69) and (70), with the one exception being that Δt in Eq. (67) must be replaced by $(1 - \lambda_2)\Delta t$.

(5)   Numerical Letermination at an Interior Point
Near the Shock Wave

This is the final type of point which must be considered and is shown in Figure 16.
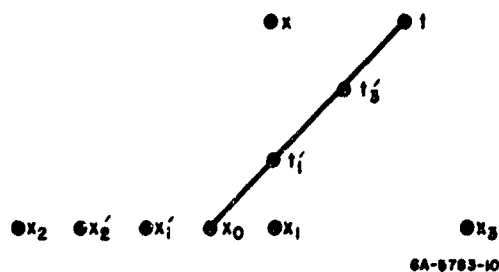
FIG. 16 INTERIOR POINT
NEAR THE SHOCK WAVE

In this the points x_0 and $\bar{x}$ are on the shock wave, but the points x_1 and x_3 may both lie to the right of the shock wave or only x_3 may lie to the right. In any event, x_2 will lie to the left.

The coordinate of x_2' is found by

$$x_2' = - \frac{[(v + c)(x_2) + (v + c)(x_0)]}{2} \Delta t + x$$

and

$$\lambda_2 = \frac{x_2' - x}{x_0 - x_2}$$

if x_0 lies to the left of x or x_1.

If x_0 lies to the right of x_0 or x, then x_1 is used in place of x_0 in the above equation. Again the field quantities at x_2' are found by Eq. (60).

If x_0 lies to the right of x_1, then x_1' and the field quantities at x_1' are computed as for the general interior point. If x_0 lies to the left of x_1, then x_1' may lie either to the left of or right of x_0.

Thus for $x_0 < x_1$, x_1' is first computed from the formula

$$x_1' = - \frac{[v(x_2) + v(x_0)]}{2} \Delta t + x$$

and

$$\lambda_1 = \frac{x_1' - x_2}{x_0 - x_2}$$

57

if x_1' is less than x_0. If the above is true, the field quantities at x_1' are then found by application of Eq. (60). If, however, x_1' lies to the right of x_0, the quantity t_1' must be computed through the formula

$$t_1' = \frac{\left[\dfrac{v(x_0) + v(\bar{x})}{2}\right] t'(x) - U(x_0)t(x_0) + x_0 - x}{\left[\dfrac{v(x_0) + v(x)}{2}\right] - U(x_0)}$$

and

$$\lambda_1 = \frac{t_1' - t(x_0)}{\Delta t} \quad .$$

The field quantities at t_1' are found from Eq. (60) with A being x_0 and and B replaced by $\bar{x}$.

For x_3' several cases may also occur. We note, first, that the case when x_3 lies to the left of x_0 corresponds to x being a general interior point; therefore, we assume that $x_3 > x_0$. We first compute x_3' from

$$x_3' = \frac{[(v - c)(x_0) + (v - c)(\bar{x})]}{2} \Delta t + x$$

and if $x_3' \leq x_0$,

$$\lambda_3 = \frac{x_3' - x_2}{x_0 - x_2}$$

and the field quantities are readily found through Eq. (60).

If $x_3' > x_0$, the quantity t_3' can be computed from

$$t_3' = \frac{U(x_0)t(x_0) + x - x_0 - \left\{\dfrac{(v - c)(x_0) + (v - c)(\bar{x})}{2}\right\} t(x)}{U(x_0) - \left\{\dfrac{(v - c)(x_0) + (v - c)(\bar{x})}{2}\right\}}$$

and

$$\lambda_3 = \frac{t_3' - t(x_0)}{\Delta t} \quad .$$

58

The values of the field quantities at t_3' are then found again from Eq. (60) with the appropriate but obvious substitutions.

This completes the method of computation at all points except the initial point.

(6) Initial Values

In order to determine the initial values we use the boundary conditions and the jump conditions across the shock wave. $p_x(x)$ or $v(x)$ is known at the initial point. Then Eqs. (81), (82), and (84) can be used to determine the remaining three of the four quantities $U(x)$, $v(x)$, $p(x)$, and $\rho(x)$. Again the equations are reduced to a single equation in $\rho(x)$ and the resulting equation is solved by the method of Newton. This method has been programmed into the digital computer Burroughs 5500 and IBM 7090.

c. Method of von Neumann and Richtmyer

The equations of motion and the constitutive relationships can be rewritten as

$$\rho\dot{v} = \frac{\partial \sigma_x}{\partial x} = \frac{\partial}{\partial x}(-p + D_{xx}) \tag{87}$$

$$-\frac{\dot{\rho}}{\rho} = \frac{\partial v}{\partial x} \tag{88}$$

$$p = f(\rho) \tag{89}$$

$$\frac{\dot{D}_{xx}}{2G} \cdot \frac{D_{xx} - \theta y}{2GT} = \dot{\epsilon}_x = \frac{\partial v}{\partial x} \; . \tag{90}$$

These equations apply only when $|D_{xx}| \geq y$. In these equations, the dots are the time derivatives along the particle path. A simple one-parameter relaxation model has been assumed, for purposes of discussion. Other models can be treated in this way.

One of the methods of integration of the partial differential equations of the type expressed in Eqs. (87) to (90) is the method of von Neumann and Richtmyer (Refs. 14,15), sometimes called the "Q" method.

59

In this method, finite difference forms of the differential equations are used. The necessity of locating the shock position and of applying the appropriate jump conditions across these shock waves is eliminated by introducing a stress term defined as artificial viscous stress Q. This stress is proportional to the gradient of the particle velocity and has the effect of spreading the shock discontinuities over a few cells of the finite difference network. The introduction of the viscous stress introduces an error in addition to the error caused by the finite difference approximation of the differential equation. However, this approximation, as used and demonstrated, is quite good and very useful in solving many practical problems. The amount of error can be controlled by controlling the size of finite difference network and by the minimal use of Q. The use of Q can be kept to a minimum by introducing the artificial viscosity stress only at the shock fronts. Even though the shock discontinuities are spread over a few cells of a finite difference network, the jump conditions across the shock waves are still satisfied within a degree of accuracy that can be controlled by the size of the finite difference network and the magnitude of Q. With this Q, Eq. (87) changes to

$$\rho \dot{v} = \frac{\partial}{\partial x} (-p + Q + D_{xx}) \quad . \tag{91}$$

The usual expression used for Q is

$$Q = A\rho \left(\frac{\partial p}{\partial \rho} + \frac{4G}{3\rho} \right)^{\frac{1}{2}} \frac{\partial v}{\partial x} \Delta x \tag{92}$$

where A is a constant. Then

$$\rho \dot{v} = \frac{\partial}{\partial x} \left[-p + A \left(\frac{\partial p}{\partial \rho} + \frac{4G}{3\rho} \right)^{\frac{1}{2}} \frac{\partial v}{\partial x} \Delta x + D_{xx} \right] \quad . \tag{93}$$

It is the stress term proportional to $\partial v / \partial x$ that provides dissipation and spreading of the shock wave.

d. Modified Q Method

In the problem of wave propagation in stress-relaxing solids, the dissipation is built in through the constitutive relations. This

dissipation, which comes through the physical mechanism of stress relaxation, can take the place of the artificially introduced Q in the method of von Neumann. This can be seen in the following way. Equation (90) can be simplified to yield

$$D_{xx} = 2GT \frac{\partial v}{\partial x} - T\dot{D}_{xx} + \theta y \quad . \tag{94}$$

This equation and Eq. (87) yield

$$\rho\dot{v} = \frac{\partial}{\partial x} \left(-p + \theta y - T\dot{D}_{xx} + 2GT \frac{\partial v}{\partial x} \right) \quad . \tag{95}$$

Equation (95) contains a term proportional to $\partial v/\partial x$, just as in Eq. (93). This can provide the spreading of the plastic shock wave. Thus we have a dissipation term from the physical mechanism rather than an artificial one. However, in starting the process of integration an artificial Q is needed until the calculated stress deviator terms are sufficient to take care of stabilizing the procedure of numerical integration.

The stability and convergence of such methods are discussed in Refs. 15 and 16.

Finite difference equations and the coding used in numerical integration are similar to those discussed by Wilkins (Ref. 17).

4. Decay of the Elastic Precursor

The decay of pressure at the elastic shock front can be calculated in a stress-relaxing material under restrictive assumptions. The model for this discussion will be the one-dimensional Zener type of macroscopic relaxing material. As discussed in Section III-2-b(1), the constitutive relation for this material will be

$$\dot{p}_x - c^2 \dot{\rho} = F'(\rho, \sigma_x) \quad .$$

A restrictive assumption which makes some analytical calculation possible is that the $p_x - \rho$ relationship in the unrelaxed (i.e., elastic) material is given by

$$p_x = A\left(1 - \frac{\rho_0}{\rho}\right) \quad . \tag{96}$$

This relationship is similar to the hydrodynamic type of relationship. It will introduce a very serious restriction on the application of the results; however, a trend might be indicated.

Along the leading characteristic α,

$$\frac{dp_x}{dt} + \rho c \frac{dv}{dt} = -F' \tag{97}$$

and the path of the characteristic α is defined by

$$\frac{dx}{dt} = v + c \quad . \tag{98}$$

The constant A can be written as

$$A = \rho_0 U_0^2 \tag{99}$$

where U_0 is a quantity with dimensions of velocity.

At the front-running shock wave in a relaxing material the jump conditions are elastic. Then the front-running shock velocity U can be calculated from the jump conditions.

$$U^2 = \frac{P_x}{\rho_0\left(1 - \dfrac{\rho_0}{\rho}\right)} \quad . \tag{100}$$

From Eqs. (98) and (99)

$$U_0^2 = \frac{P_x}{\rho_0\left(1 - \dfrac{\rho_0}{\rho}\right)} \quad . \tag{101}$$

Hence

$$U = U_0 \quad . \tag{102}$$

Then the jump condition expressing the conservation of mass yields the particle velocity

$$V = U_0\left(1 - \frac{\rho_0}{\rho}\right) \tag{103}$$

$$c^2 = \frac{dp_x}{d\rho} = \left(\frac{\rho_0 U_0}{\rho}\right)^2 \quad , \quad c = \frac{\rho_0 U_0}{\rho} \quad . \tag{104}$$

The path of the leading characteristic α can be calculated from Eq. (97)

$$\left(\frac{dx}{dt}\right)_\alpha = v + c = U_0 \quad . \tag{105}$$

Thus the leading characteristic α and the front-running (or elastic) shock wave coincide. Along the elastic shock wave the compatibility equation [Eq. (97)] corresponding to the α characteristic is valid. By using the expression for c from Eq. (104), Eq. (97) becomes

$$\frac{dp_x}{dt} + \rho_0 U_0 \frac{dv}{dt} = -F' \quad . \tag{106}$$

Along the front-running shock wave the jump conditions yield

$$P_x = \rho_0 U v = \rho_0 U_0 v \quad . \tag{107}$$

63

Then Eq. (106) becomes

$$\frac{dp_x}{dt} = -\frac{F'}{2} \ . \tag{108}$$

This equation gives the rate of decay at the wave front. If F' is given by

$$F' = \frac{p_x - p_i}{T} \ . \tag{109}$$

Then

$$\frac{dp_x}{dt} = -\frac{p_x - p_i}{2T} \tag{110}$$

$$\frac{dp_x}{p_x - p_i} = -\frac{1}{2T} \, dt \tag{111}$$

and

$$p_x = p_i + Be^{-t/2T} \tag{112}$$

where B is an arbitrary constant. The constants B and T can be determined from experimental results. If F' is given by

$$F'(\rho,\sigma_x) = \frac{p_x - p_i(\sigma_x,\rho)}{T_1}$$

and

$$\dot{p}_i = \left[\frac{p_i - \bar{p}}{T_2}\right] \tag{113}$$

then

$$\frac{dp_x}{dt} = -\frac{1}{2}\left[\frac{p_x - p_i}{T_1}\right] \tag{114}$$

$$p_i = \bar{p} + [p_i(0) - \bar{p}]e^{-t/T_2} \tag{115}$$

and

$$\frac{dp_x}{dt} = -\frac{1}{2T_1}\{p_x - [p_i(0) - \bar{p}]e^{-t/T_2} - \bar{p}\} \ . \tag{116}$$

64

i.e.,

$$\frac{dp_x}{dt} + \frac{1}{2}\frac{p_x}{T_1} = \frac{[p_1(0) - \bar{p}]}{2T_1} e^{-t/T_2} + \frac{\bar{p}}{2T_1} \quad . \tag{117}$$

The solution to this differential equation is

$$p_x = A_1 e^{-t/2T} + \frac{p_i(0) - \bar{p}}{\left(1 - \frac{2T}{T_2}\right)} e^{-t/T_2} + \bar{p} \quad ,$$

If the initial amplitude of the precursor is different from the initial yield value $p_i(0)$, then A_1 is not zero and the relaxation constant T_1 takes care of the time required to relax toward the yield value and the formation of a two-wave structure. This two-wave structure is continually changing with decreasing amplitude of the precursor toward the static value. This is taken care of by the relaxation constant T_2.

These calculations are similar to the calculation by Taylor, and any evaluation of relaxation phenomena in this way is based on some very restrictive assumptions, as discussed earlier.

Any accurate evaluation of the relaxation phenomena must be based on realistic $p_x - \rho$ relationships and the models based on continuum mechanics. At present this can be done only by numerical techniques. Furthermore, these methods provide some freedom in the choice of parameters in the relaxation model, and thus the experimental results including the flow behind the wave front can be interpreted more accurately.

65

5. Discussion of Some Numerical Results

a. Wave Calculations

Experimental observations in hard and soft aluminum indicate a two-wave structure at very early times; the amplitude of the elastic wave decreases with time. The two-parameter macroscopic relaxation model was used in a modified Q code to correlate the experimental results. The properties of aluminum used in the calculation are as follows:

$$\rho_0 = 2.785 \text{ gm/cc}$$

$$p = a(\rho/\rho_0 - 1) + b(\rho/\rho_0 - 1)^2 + c(\rho/\rho_0 - 1)^3$$

$$a = 0.755 \text{ Mbar}$$

$$b = 1.29 \text{ Mbar}$$

$$c = 1.197 \text{ Mbar}$$

$$\bar{y} = 0.0025 \text{ Mbar}$$

$$G = 0.287 \text{ Mbar}$$

The relaxation constants T_1 and T_2 were introduced earlier in Section III-2-b(1). T_1 controls the rate of formation of a two-wave structure; experimental observation indicates that it should be very small. T_2 governs the rate of decay of the precursor amplitude.

The values of T_1 and T_2 used in the calculation are 0.005 and 3.72 μsec, respectively. These values were chosen by trial and error to match approximately the observed precursor decay—they do not represent a best fit. Figure 17 shows the decay of the precursor amplitude with the penetration depth. A comparison of observed and computed precursor decay is shown in Fig. 18.

The curve in Fig. 19 gives the variation of σ_x with distance for selected times when the boundary is subjected to a fixed velocity rather than a fixed stress. This curve was computed by the characteristic method for a one-parameter model; hence the profiles do not appear as two separate waves as observed experimentally. Note, however, the pronounced stress relaxation at the boundary. Computations like this are needed for the two-parameter model, so that a more direct comparison with experiment can be made.
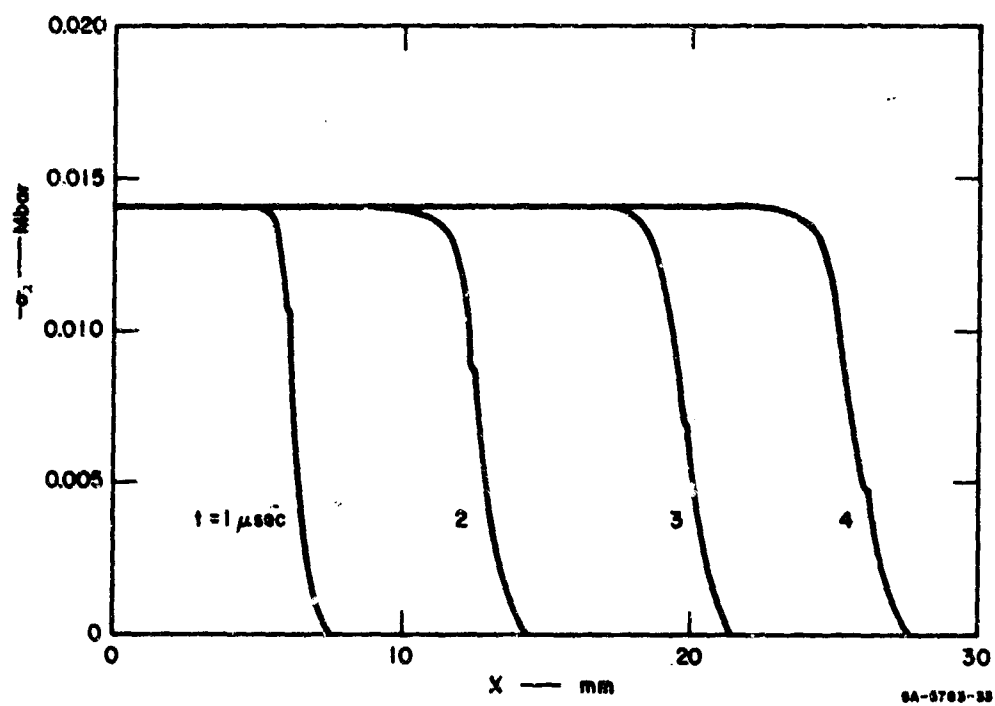
66

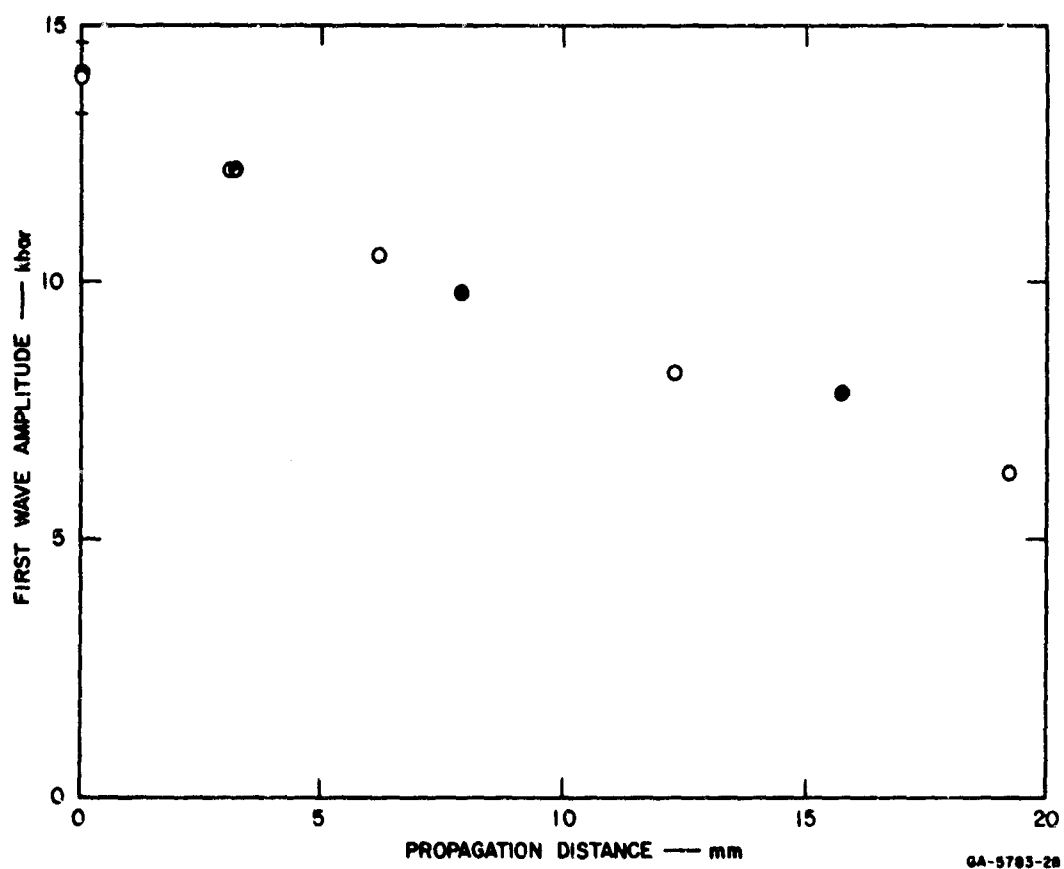FIG. 17   DECAY OF PRECURSOR WITH PENETRATION DEPTH

FIG. 18 DECAY OF ELASTIC PRECURSOR. Solid points are experimental;
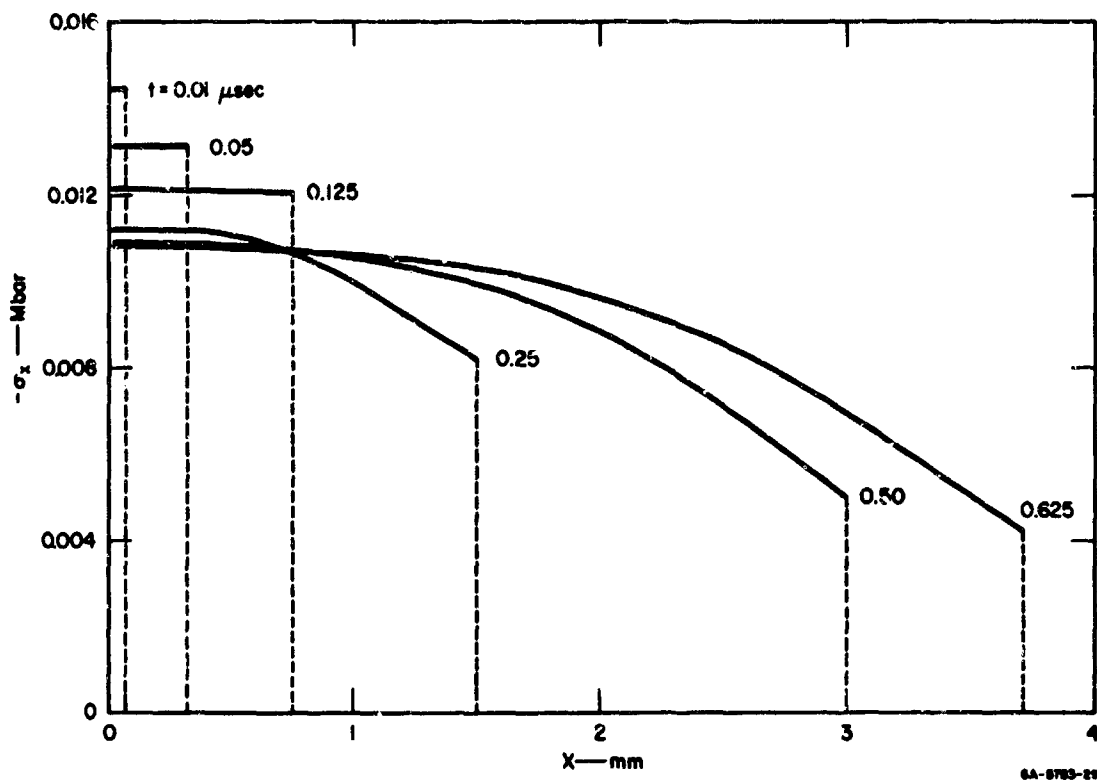open circles are computed.

FIG. 19 STRESS PROFILES FOR CONSTANT VELOCITY INPUT AT THE INTERIOR BOUNDARY

b.   Computation from the Characteristic Code

In the problem of stress relaxation we have a dissipation built in through the constitutive relations. In the modified Q method described in Section III-3-d, the artificial dissipation has been kept to a minimum; it is confined to the starting of the process of computation. However, one weakness of the method is that the elastic shock front is not clearly defined and the elastic wave amplitude cannot be predicted exactly. To overcome these deficiencies, the characteristic code is the most accurate method available. The error in this method is due only to the approximation of the differential equation by a finite difference scheme. This can be controlled by suitably selecting the finite difference mesh work, depending on the desired degree of accuracy.

Early numerical calculations were done for quartz for purposes of illustration of the stress-relaxation properties. (At the time these calculations were made, experimental results on aluminum were not available.) A one-parameter macroscopic relaxation model was used.

The $p - \rho$ relationship for quartz was assumed to be:

$$p = 0.3919 \quad (\rho/\rho_0 - 1) \text{ Mbar}$$

$$\rho_0 = 2.5 \quad \text{gm/cc}$$

Other parameters used were:

$y = 0.002$ Mbar

$G = 0.37$ Mbar

$T = 0.03 \ \mu\text{sec.}$

Figure 20 is an $x - t$ diagram showing the positions of the left boundary and the position of elastic shock front with time. Figure 21 illustrates the distribution of p_x with the Eulerian coordinate x for different values of time t. In the computation the stress on the left boundary was kept constant at 0.1 Mbar. The curves indicate the results obtained by the method of characteristics; the points illustrate the values obtained by the modified Q method.

Figure 22 illustrates the decay of the elastic shock. Figures 23 and 24 illustrate the distributions of the particle velocity and the specific volume with the Eulerian coordinate x for different values of time t.
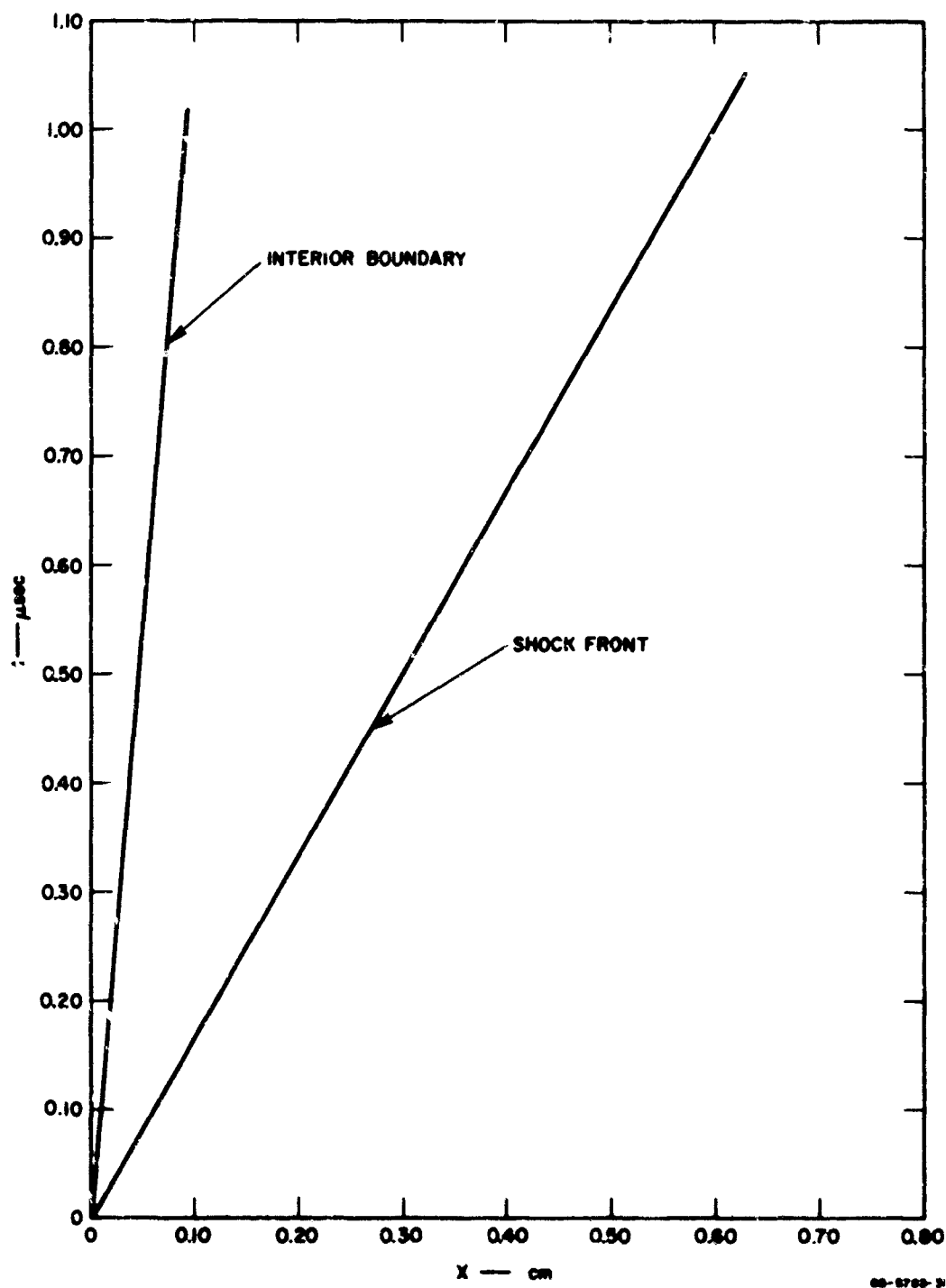
70

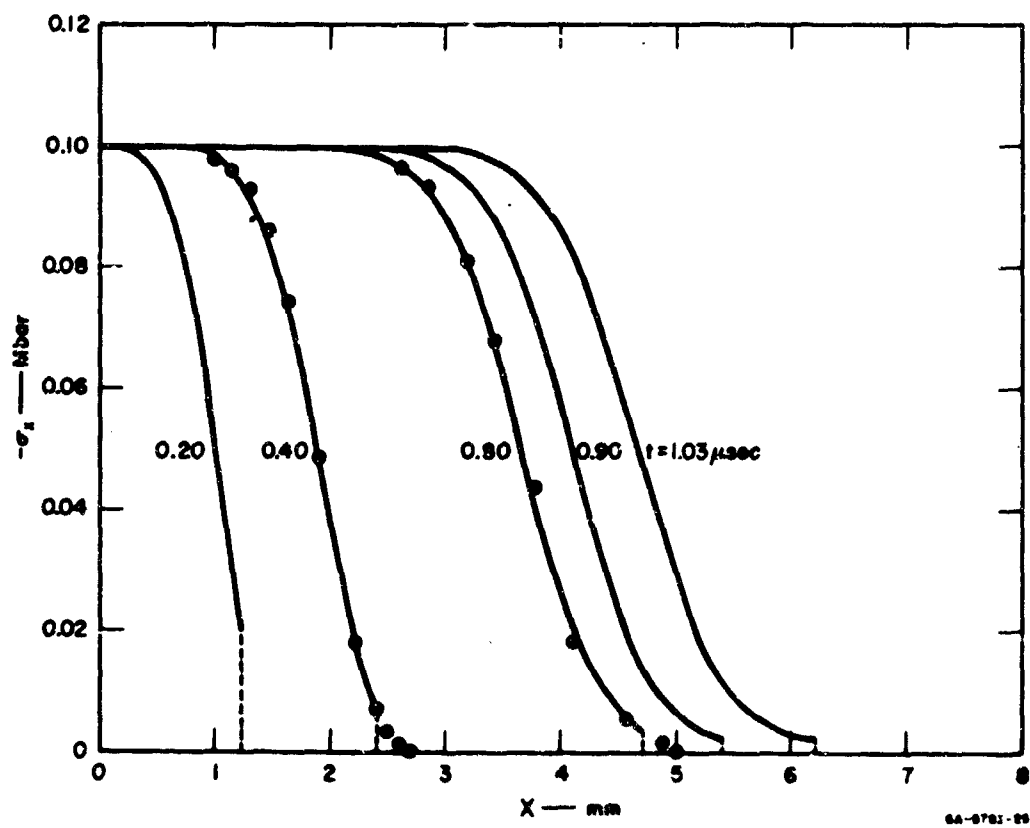FIG. 20 POSITION OF INTERIOR BOUNDARY AND SHOCK WAVE AS FUNCTIONS OF TIME

71

FIG. 21 STRESS PROFILES AT DIFFERENT TIMES. Curves from characteristic method; points from modified Q method.
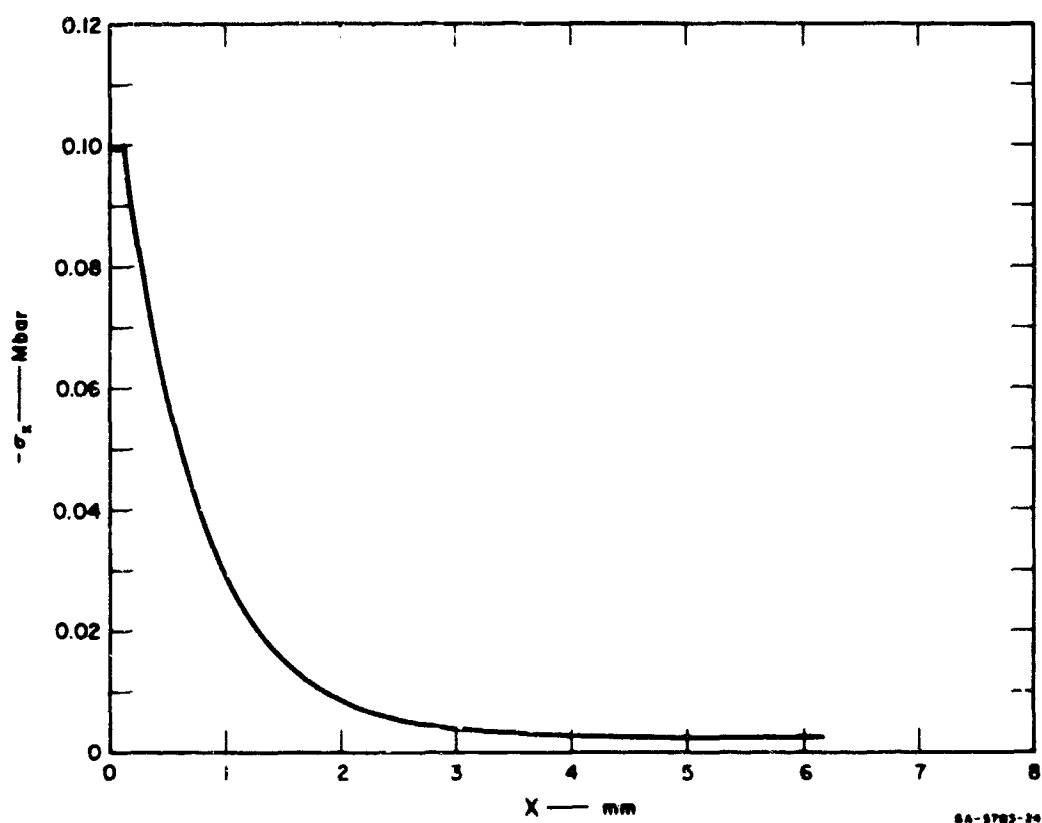
FIG. 22 DECAY OF PRECURSOR STRESS WITH PROPAGATION DISTANCE

73
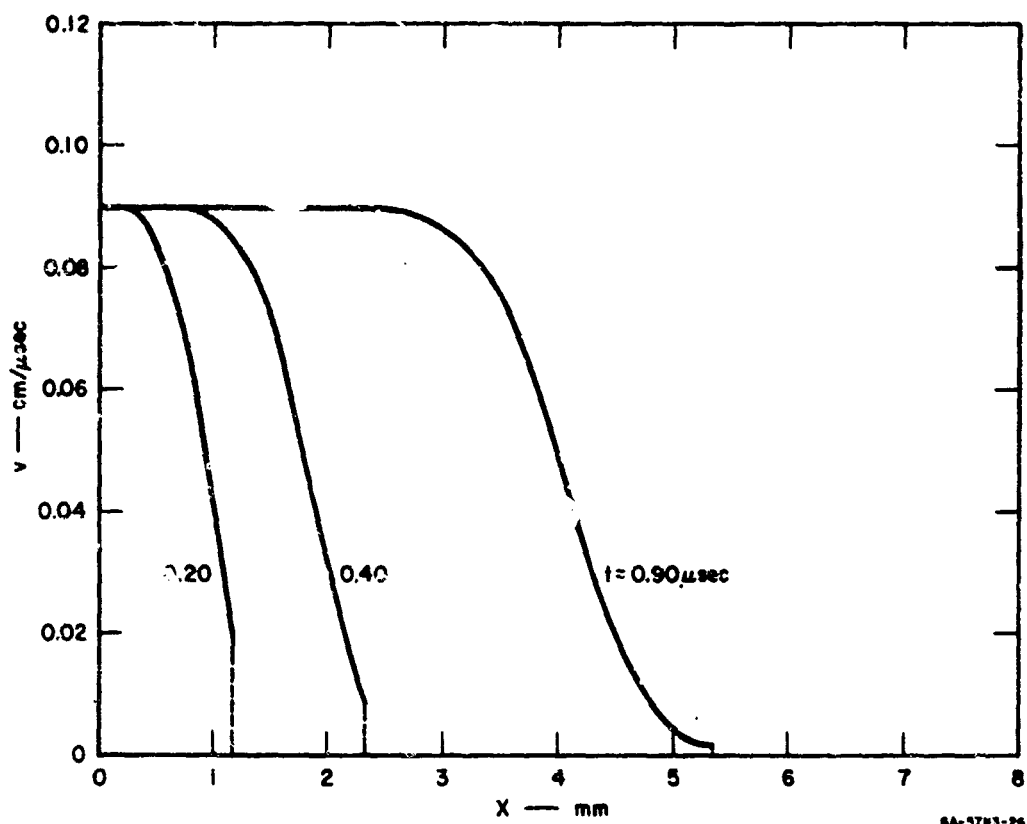
FIG. 23 PARTICLE VELOCITY PROFILES AT DIFFERENT TIMES
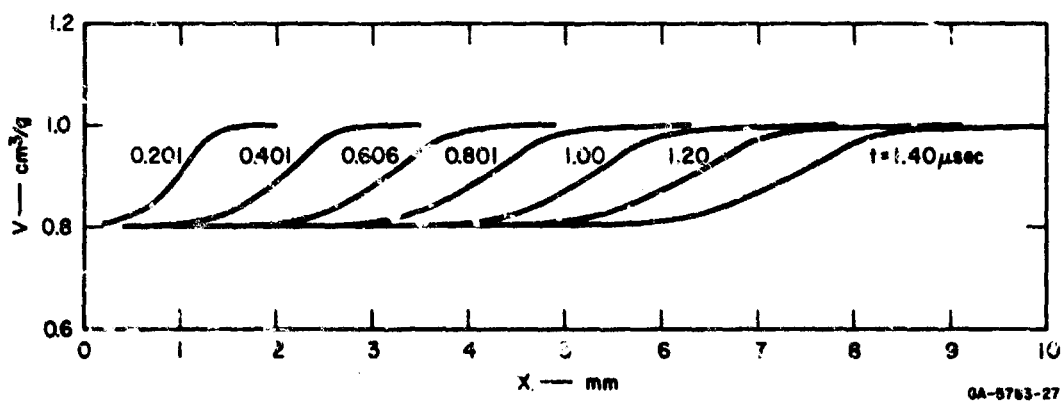
FIG. 24 SPECIFIC VOLUME PROFILES AT DIFFERENT TIMES

c. Dislocation Model

Figures 25-29 illustrate the results obtained from numerical calculations (von Neumann and Richtmyer method) when the dislocation model for stress relaxation was used [see Section III-2-b-(2)]. Again, the calculations were performed only for purposes of illustration. Iron, which exhibits pronounced stress relaxation, was used for calculations. The following values were used for the constants in the constitutive relation:

$$bN_{m\,0} = 5.0 \text{ cm}^{-1}$$

$$B = 0.0198 \text{ Mbar}$$

$$V_m = 0.\text{·}2 \text{ cm}/\mu\text{sec}$$

$$T_1 = 1.0 \ \mu\text{sec}$$

$$T_2 = 4.0 \ \mu\text{sec}$$
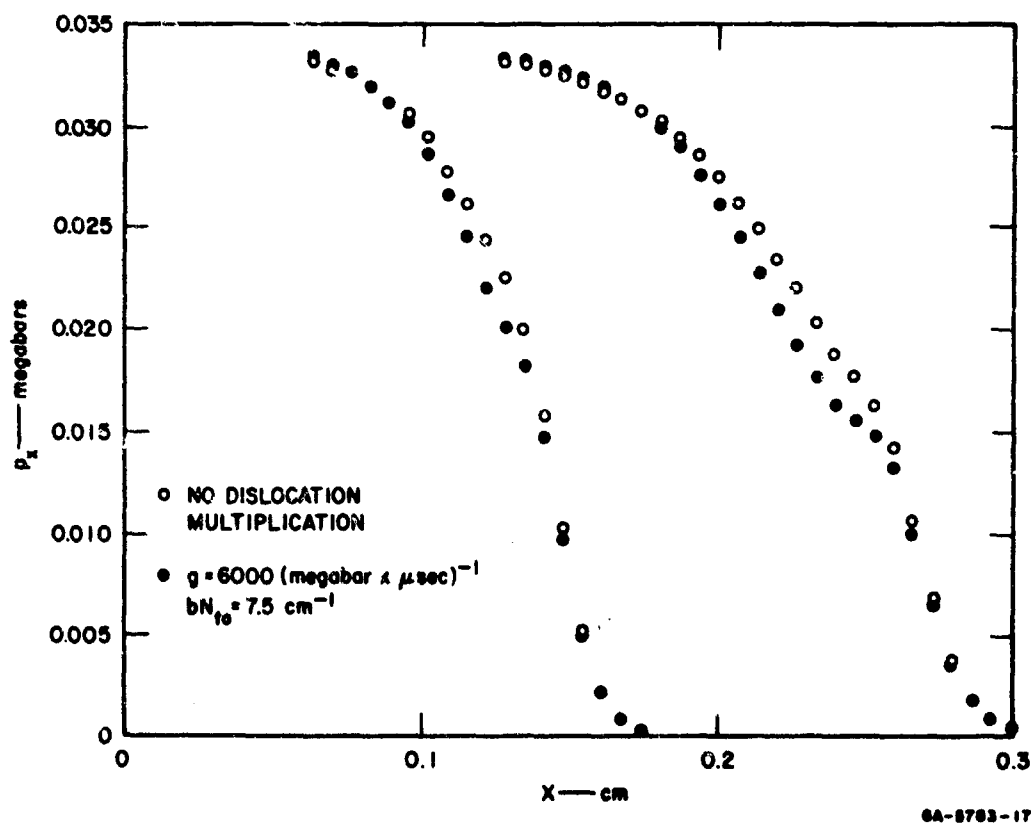
FIG. 25 SHOCK PROFILES SHOWING THE EFFECT OF DISLOCATION MULTIPLICATION
Profiles in iron at 0.25 and 0.45 μsec.
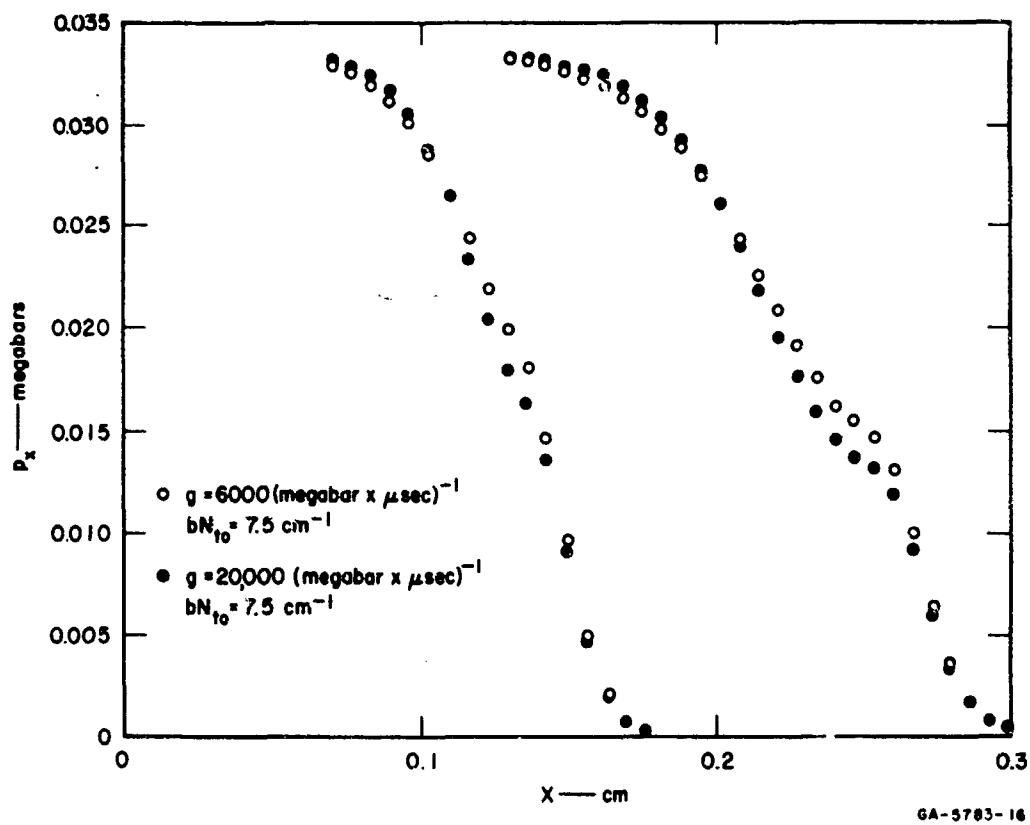
FIG. 26 SHOCK PROFILES SHOWING THE EFFECT OF INCREASING g.
Profiles in iron at 0.25 and 0.45 μsec.

76
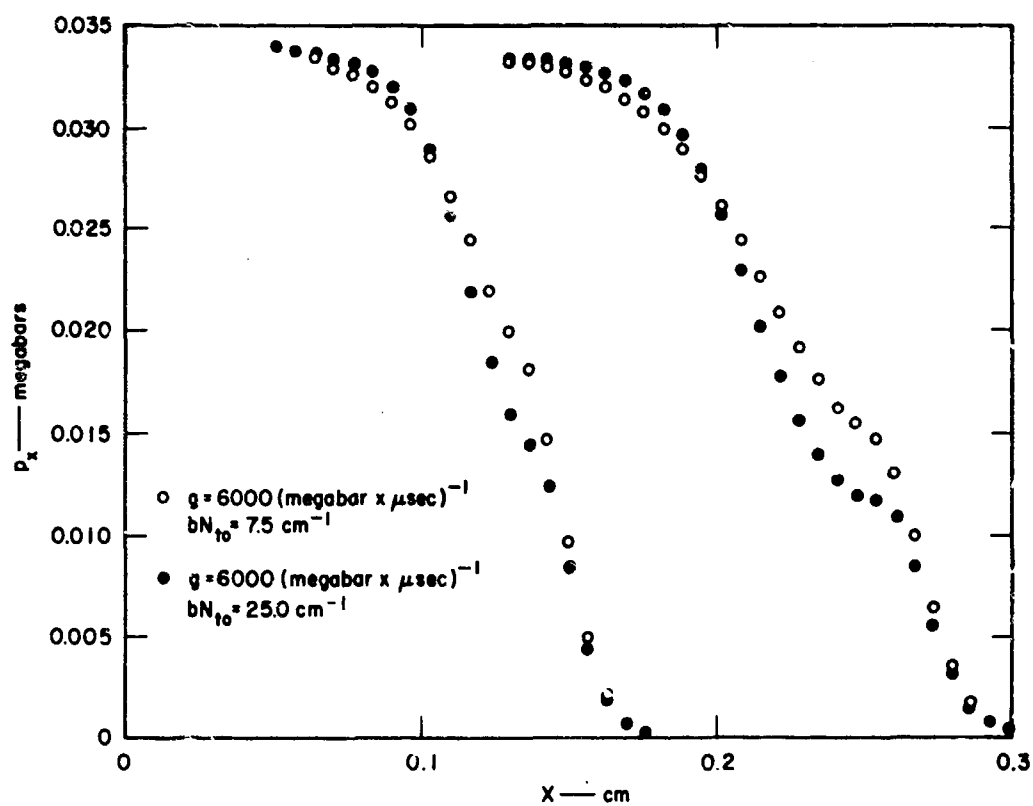
FIG. 27 SHOCK PROFILES SHOWING THE EFFECT OF INCREASING THE INITIAL DENSITY OF PINNED DISLOCATIONS. Profiles in iron at 0.25 and 0.45 μsec.

77
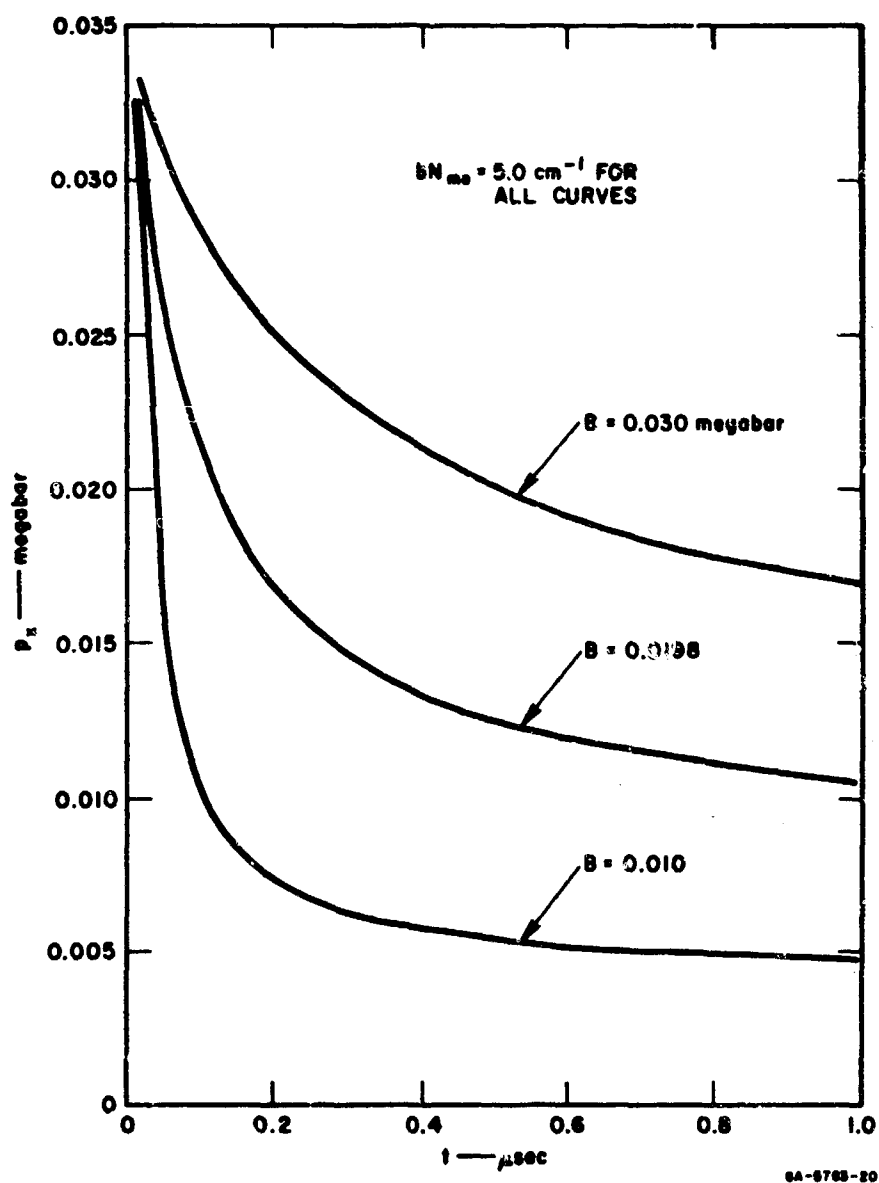
FIG. 28 PRECURSOR DECAY FOR VARIOUS VALUES OF B,
THE CONSTANT IN THE GILMAN-JOHNSTON MODEL
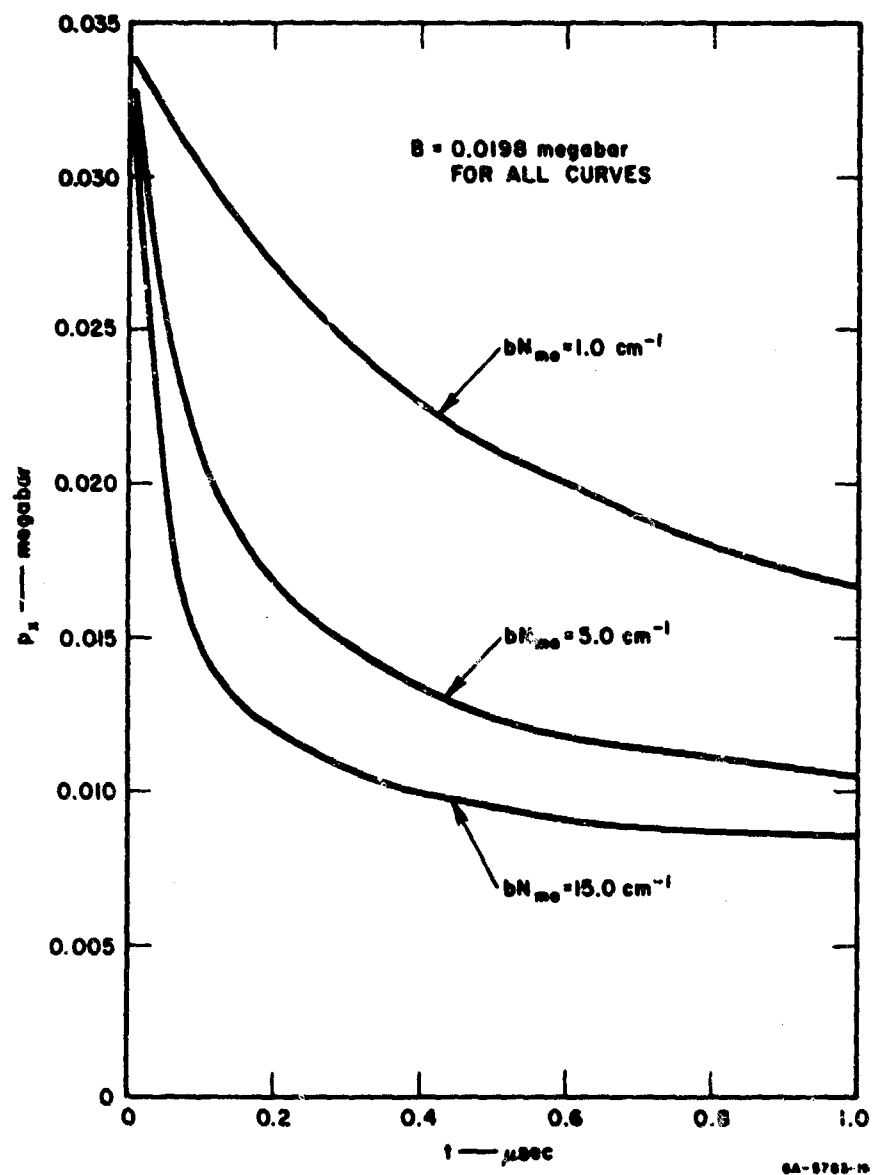
FIG.   PRECURSOR DECAY FOR VARIOUS VALUES OF THE INITIAL
         MOBILE DISLOCATION DENSITY

79

Figure 25 shows the distribution of p_z with the Eulerian coordinate x for two specific times: $t = 0.25$ μsec and $t = 0.45$ μsec. This figure illustrates the effect of dislocation multiplication; the open circles are for no dislocation multiplication, and the dots are for $g = 6000$ (Mbar-μsec)$^{-1}$ and $bN_{t0} = 7.5$ cm^{-1}. The effects of dislocation multiplication are a more pronounced elastic precursor and a steeper plastic shock wave.

Figure 26 illustrates the effect of changing g. Two values of g were used: $g = 6000$ (Mbar-μsec)$^{-1}$ and $g = 20,000$ (Mbar-μsec)$^{-1}$. A value of 25 cm^{-1} was used for bN_{t0} in both cases. The higher value of g reduced the precursor amplitude significantly.

Figure 27 illustrates the variation of bN_{t0} for a fixed value of g of 6000 (Mbar-μsec)$^{-1}$. Two values of bN_{t0},

$$bN_{t0} = 7.5 \text{ cm}^{-1}$$

and

$$bN_{t0} = 25.0 \text{ cm}^{-1} \qquad \text{are compared.}$$

The larger value of bN_{t0} has the lower amplitude of elastic precursor.

Figures 28 and 29 illustrate the decay of the amplitude of the elastic shock wave with time for different values of B and $N_{\bullet 0}$.

These parameter studies illustrate the effect of various material constants on shock propagation.

d. Attenuation of Peak Pressure

One of the important problems of practical interest is the attenuation of peak pressure of a pulse of finite duration. A study of this phenomenon requires a knowledge of the unloading behavior and the constitutive relations during unloading. The constitutive relations for loading are now understood in some cases where stress relaxation is present, however, there are no experimental data available on unloading under conditions such that stress relaxation is important.

To obtain some information regarding the trend that the decay of peak pressure might follow when stress relaxation is present, the following calculation has been performed. It has been assumed that the relaxing constitutive relation is the same in loading as well as in unloading. The material and the constants used are the same as in the case of the computation with the characteristic code. A pressure of 0.1 Mbar is applied at time $t = 0$; the subsequent loading history is shown in Fig. 30. This figure illustrates the decay of peak pressure with time. The dashed line corresponds to elastic-plastic theory without stress relaxation.
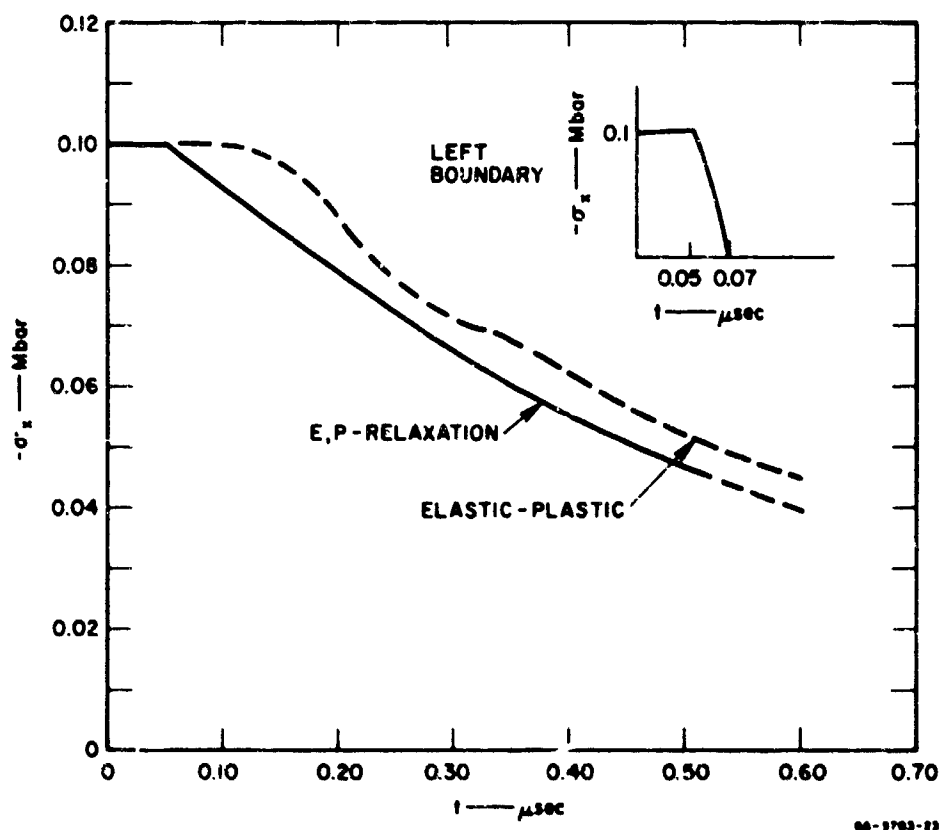

FIG. 30 CALCULATED DECAY OF PEAK PRESSURE IN ALUMINUM WITH AND WITHOUT STRESS RELAXATION

81

6. Summary

In summary, the major results of the theoretical part of this contract are the development of a mathematical model of stress relaxation, together with numerical results on the rate of decay of the elastic precursor wave, and some computed wave profiles. The numerical results have been correlated with experimental results and it is shown that the two-parameter model of stress relaxation predicts experimental results more accurately than the one parameter model. The computations have been performed using the method of characteristics and the so-called "Q" method of von Neumann and Richtmyer. The reasons for the expenditure of effort on the method of characteristics are:

1. The method is more accurate than the "Q" method. It was therefore possible to study the effect of stress relaxation in the absence of artificial viscosity, then to use the "Q" method to study stress relaxation, and to compare the difference in the results obtained by the two methods.

2. The "Q" method is highly inaccurate for situations involving reflected waves; however, results obtained by the method of characteristics can be used to indicate correction terms which could be added to "Q" method codes.

Another result of the present work is that the term involving stress relaxation provides a real viscosity and hence the artificial viscosity term may be omitted from "Q" codes when stress relaxation is present. It should be pointed out that the stress relaxation models employed here are most applicable to metals and it is quite possible that thermodynamic effects will be of greater importance in plastics than stress relaxation; this point requires further study.

It is to be noted that the basic differential equations used in the present work differ from those used in the PUFF codes only in the constitutive relations which are used. It is not a difficult matter to incorporate the stress relaxation model into a PUFF code. Some work on expansion of the models and more correlation with experimental results should be accomplished before these models are used.

APPENDIX I

SHOTS FIRED DURING THIS PROGRAM

APPENDIX I

SHOTS FIRED DURING THIS PROGRAM

All the shots fired under the present contract are listed below, with an indication of the purpose for firing each shot. Some shots were of a development nature and did not contribute significant data points.

APPENDIX I

SHOT NO.	TYPE OF GAGE	PURPOSE
12,810	Quartz	Calibration of quartz gages
12,812	Quartz	Calibration of quartz gages
12,813	Quartz	Calibration of quartz gages
12,811	2 Quartz	Development of technique to mount quartz in projectile
12,053	Quartz	Look for elastic wave in Plexiglas
12,052	Quartz	Look at elastic wave in stock 2021 aluminum
12,050	Manganin[a]	Look at elastic wave in stock 2024 aluminum
12,051	Manganin[b]	Look at elastic wave in stock 2024 aluminum
12,172	Quartz	Study elastic wave in annealed 2024 aluminum
12,168	Quartz	Study elastic wave in annealed 2024 aluminum
12,170	Quartz	Study elastic wave in annealed 2024 aluminum
12,175	Quartz	Study elastic wave in annealed 2024 aluminum
12,169	Quartz	Study elastic wave in annealed 2024 aluminum
12,807	Quartz	Study elastic wave in hardened 2024 aluminum and look for plastic wave decay
12,808	Quartz	Study elastic wave in hardened 2024 aluminum and look for plastic wave decay
12,173	Quartz	Study elastic wave in hardened 2024 aluminum
12,171	Quartz	Study elastic wave in hardened 2024 aluminum
12,174	Quartz	Study elastic wave in hardened 2024 aluminum
12,511	Manganin	Study wave profile in polyethylene
12,512	2 Manganin	Study wave profile in polyethylene
12,513	2 Manganin	Study wave profile in polyethylene
12,514	2 Manganin	Study wave profile in polyethylene
12,515	2 Manganin	Study wave profile in polyethylene
12,516	2 Manganin	Study wave profile in polyethylene
12,517	2 Manganin	Study wave profile in polyethylene
12,804	2 Manganin	Study wave profile in polyethylene
12,805	2 Manganin	Study wave profile in polyethylene
12,806	2 Manganin	Study wave profile in polyethylene

[a] Manganin wire electrically insulated from Al plate by 0.001-inch Mylar foil and potted in C-7 epoxy.

[b] Manganin wire insulated with 0.001-inch Mylar and surrounded by aluminum blocks.

APPENDIX II

CHARACTERISTIC EQUATION BASED ON THE EXISTENCE
THEOREM OF CAUCHY-KOWALEWSKI

CHARACTERISTIC EQUATION BASED ON THE EXISTENCE
THEOREM OF CAUCHY-KOWALEWSKI (Ref. 18)

We begin with the equations expressing conservation of mass and momentum

$$\frac{\partial \sigma_x}{\partial x} - \rho \left(\frac{\partial v}{\partial t} + v \frac{\partial v}{\partial x} \right) = 0 \tag{1}$$

$$\frac{\partial \rho}{\partial t} + v \frac{\partial \rho}{\partial x} + \rho \frac{\partial v}{\partial x} = 0 \tag{2}$$

We write the constitutive relations in the form

$$p = -\left(\frac{\sigma_x + 2\sigma_y}{3} \right) = \bar{f}(\rho) \tag{3}$$

$$\frac{2}{3} \frac{\partial v}{\partial x} + \frac{1}{2G} \left[\frac{\partial S_1}{\partial t} + v \frac{\partial S_1}{\partial x} \right] = g(S_1 - \theta Y) \tag{4}$$

where

$$S_1 = 2 \left(\frac{\sigma_x - \sigma_y}{3} \right) \quad , \qquad g = \frac{1}{2GT}$$

These equations may be conveniently rewritten in the form

$$\frac{\partial S_1}{\partial x} - \frac{\partial p}{\partial x} - \rho \left(\frac{\partial v}{\partial t} + v \frac{\partial v}{\partial x} \right) = 0 \tag{5}$$

$$\frac{\partial \rho}{\partial t} + v \frac{\partial \rho}{\partial x} + \rho \frac{\partial v}{\partial x} = 0 \tag{6}$$

$$\frac{\partial p}{\partial t} + v \frac{\partial p}{\partial x} - \frac{d\bar{f}}{d\rho} \left(\frac{\partial \rho}{\partial t} + v \frac{\partial \rho}{\partial x} \right) = 0 \tag{7}$$

$$\frac{2}{3}\frac{\partial v}{\partial x} + \left[\frac{1}{2G}\frac{\partial S_1}{\partial t} + v\frac{\partial S_1}{\partial x}\right] = g(S_1 - \theta Y) \qquad (8)$$

Although many equivalent definitions of characteristics are possible, we adapt here the one based on the existence proof of Cauchy-Kowalewski. The reason for this choice is that it gets us to the desired goal along the most direct path.

We omit obvious details and proceed to look for curves $f(x,t) =$ constant, along which the set of Eqs. (5) - (8) cannot be solved as an algebraic system for the partial derivatives $\partial S_1/\partial f$, $\partial p/\partial f$, $\partial v/\partial f$ and $\partial_t \partial f$.

Since

$$\frac{\partial S_1}{\partial x} = \frac{\partial S_1}{\partial f}\frac{\partial f}{\partial x} + \frac{\partial S_1}{\partial f}\frac{\partial f}{\partial t}$$

etc., we obtain the following set of equations:

$$\frac{\partial S_1}{\partial f}\frac{\partial f}{\partial x} - \frac{\partial p}{\partial f}\frac{\partial f}{\partial x} - \rho\frac{\partial v}{\partial f}\left(\frac{\partial f}{\partial t} + v\frac{\partial f}{\partial x}\right) = 0$$

$$\frac{\partial \rho}{\partial f}\left(\frac{\partial f}{\partial t} + v\frac{\partial f}{\partial x}\right) + \rho\frac{\partial v}{\partial f}\frac{\partial f}{\partial x} = 0$$

$$\frac{\partial p}{\partial f}\left(\frac{\partial f}{\partial t} + v\frac{\partial f}{\partial x}\right) - \frac{d\overline{f}}{d\rho}\frac{\partial \rho}{\partial f}\left(\frac{\partial f}{\partial t} + v\frac{\partial f}{\partial x}\right) = 0$$

$$\frac{2}{3}\frac{\partial v}{\partial f}\frac{\partial f}{\partial x} + \frac{1}{2G}\frac{\partial S_1}{\partial f}\left(\frac{\partial f}{\partial t} + v\frac{\partial f}{\partial x}\right) - g(S_1 - GY) = 0$$

The matrix of the coefficients of

$$\frac{\partial S_1}{\partial x}, \quad \frac{\partial p}{\partial f}, \quad \frac{\partial \nu}{\partial f}, \quad \text{and} \quad \frac{\partial v}{\partial f}$$

is

$$
\begin{bmatrix}
\dfrac{\partial f}{\partial x} & -\dfrac{\partial f}{\partial x} & 0 & -\rho\left(\dfrac{\partial f}{\partial t} + v\dfrac{\partial f}{\partial x}\right) \\[2ex]
0 & 0 & \left(\dfrac{\partial f}{\partial t} + v\dfrac{\partial f}{\partial x}\right) & \rho\dfrac{\partial f}{\partial x} \\[2ex]
0 & \left(\dfrac{\partial f}{\partial t} + v\dfrac{\partial f}{\partial x}\right) & -\dfrac{d\overline{f}}{d\rho}\left(\dfrac{\partial f}{\partial t} + v\dfrac{\partial f}{\partial x}\right) & 0 \\[2ex]
\dfrac{1}{2G}\left(\dfrac{\partial f}{\partial t} + v\dfrac{\partial f}{\partial x}\right) & 0 & 0 & \dfrac{4}{3}\dfrac{\partial f}{\partial x}
\end{bmatrix} = 0
$$

and the determinant of this matrix is

$$
\left(\frac{\partial f}{\partial t} + v\,\frac{\partial f}{\partial x}\right)^2 \left[\frac{\rho}{2G}\left(\frac{\partial f}{\partial t} + v\,\frac{\partial f}{\partial x}\right)^2 - \frac{2}{3}\left(\frac{\partial f}{\partial x}\right)^2 - \frac{\rho}{2G}\,\frac{d\overline{f}}{d\rho}\left(\frac{\partial f}{\partial x}\right)^2\right] \quad .
$$

There will be no solution for $\partial S_1/\partial f$ etc. if this determinant vanishes. On $f = $ constant $\partial f/\partial t = -(\partial f/\partial x)(dx/dt)$ so that the determinant vanishes when

$$
\frac{dx}{dt} = v, \; v, \; v \pm \sqrt{\frac{d\overline{f}}{d\rho} + \frac{4G}{3\rho}} \quad . \tag{9}
$$

The four roots given by Eq. (9) are the characteristics of the governing differential equations.

APPENDIX III

COMPATIBILITY CONDITIONS

APPENDIX III

COMPATIBILITY CONDITIONS

The governing differential equations are:

$$\frac{\partial S_1}{\partial x} - \frac{\partial p}{\partial x} - \rho \left(\frac{\partial v}{\partial t} + v \frac{\partial v}{\partial x} \right) = 0 \tag{1}$$

$$\frac{\partial \rho}{\partial t} + v \frac{\partial \rho}{\partial x} + \rho \frac{\partial v}{\partial x} = 0 \tag{2}$$

$$\frac{\partial S_1}{\partial t} + v \frac{\partial S_1}{\partial x} - \frac{4G}{3} \frac{\partial v}{\partial x} = 2Gg(S_1 - \theta Y) \tag{3}$$

$$\frac{\partial p}{\partial t} + v \frac{\partial p}{\partial x} - f'(\rho) \left(\frac{\partial \rho}{\partial t} + v \frac{\partial \rho}{\partial x} \right) = 0 \quad . \tag{4}$$

The four characteristics are:

$$\frac{dx}{dt} = v_1, v_1, v \pm c$$

where

$$c = \sqrt{\frac{d\bar{f}}{d\rho} + \frac{4G}{3\rho}} \quad .$$

If we multiply Eq. (1) by c, add Eq. (3) and subtract Eq. (4), we obtain

$$\frac{\partial}{\partial t} (S_1 - p) + (v + c) \frac{\partial}{\partial x} (S_1 - p) - \rho c \left(\frac{\partial v}{\partial t} + v \frac{\partial v}{\partial x} \right) - \frac{4G}{3} \frac{\partial v}{\partial x} - \rho f'(\rho) \frac{\partial v}{\partial x} + 2Gg(S_1 - \theta Y) \quad .$$

Then using Eq. (2) we get

$$\frac{\partial}{\partial t}(S_1 - p) + (v + c)\frac{\partial}{\partial x}(S_1 - p) - \rho c\left[\frac{\partial v}{\partial t} + (v + c)\frac{\partial v}{\partial x}\right] = 2Gg(S_1 - \theta Y).$$

Thus we have

$$d(S_1 - p) - \rho c\, dv - 2Gg(S_1 - \theta Y)dt = 0 \qquad (5)$$

along

$$\frac{dx}{dt} = v + c$$

and

$$d(S_1 - p) + \rho c\, dv - 2Gg(S_1 - \theta Y)dt = 0 \qquad (6)$$

along

$$\frac{dx}{dt} = v - c \quad .$$

By using Eq. (2) in Eq. (3) we get

$$dS_1 + \frac{4G}{3\rho}\, dp - 2Gg(S_1 - \theta Y)dt = 0 \qquad (7)$$

along

$$\frac{dx}{dt} = v$$

and Eq. (4) can be written directly as

$$dp - c^2 d\rho = 0 \qquad (8)$$

along

$$\frac{dx}{dt} = v \quad .$$

Equations (5), (6), (7), and (8) are the compatibility equations for a stress-relaxing medium.

REFERENCES

1. Fowles, G. R., "Shock Wave Compression of Hardened and Annealed 2024 Aluminum," J. Appl. Phys. **32**, 1475 (1961).

2. Linde, R. K. and D. N Schmidt, "Measuring the Submicrosecond Response of Shock-Loaded Materials," Ref. Sci. Inst. **37**, 1 (1966).

3. Keough, D. D. and W. Wilkinson, "Manganin-Wire Shock-Transducer Investigation," AFWL-TR-65-170, December, 1965.

4. Halpin, W. J. and R. A. Graham, "Shock Wave Compression of Plexiglas from 3 to 20 Kilobars," Fourth Symposium on Detonation, U.S. Naval Ordnance Laboratory, October, 1965.

5. Wagner, M. H., W. F. Waldorf, and N. A. Louie, "Determination of Hugoniot Equations-of State for Polymers and Reentry Vehicle Materials and Investigations of Fractured Phenomena," AFSWC-TDR-62-66, Vol. I, August 1962.

6. Taylor J. W., J. Appl. Phys. **36**, 3146 (1965).

7. Barker, L. M., C. D. Lundergan, and W. Herrmann, J. Appl. Phys. **35**, 1203-1212 (1964).

8. Ahrens, T. J. and V. G. Gregson, Jr., J. Geophys. Res. **69**, 4839-4874 (1964).

9. Ahrens, T. J. and G. E. Duvall, J. Geophys. Res. **71**, 18. 4349-4360 (1966).

10. Duvall, G. E. "Propagation of Plane Shock Waves in a Stress Relaxing Medium," Proc. Int. Symposium on Stress Waves in Anelastic Solids, Brown University, 1963.

11. Noll, W. and C. Truesdell, "The Nonlinear Field Theory of Mechanics," *Encyclopedia of Physics*, S. Flugge, ed., 1964.

12. Gilman, J. J. and W. G. Johnston, *Solid State Physics*, Academic Press Inc., New York, 1962, Vol. 13.

13. Courant. R. and K. O. Friedrichs, *Supersonic Flow and Shock Waves*, Interscience Publishers, New York, 1948.

14. von Neumann, R. and R. D. Richtmyer, J. Appl. Phys. **21**, 232-237 (1950).

15. Richtmyer, R. D., "Difference Methods for Initial Value Problems," Interscience Tracts in Pure and Applied Mathematics No. 4, 1957.

16. Alder, B., S. Fernback, and M. Rotenberg. eds. *Methods in Computational Physics - Fundamental Methods in Hydrodynamics*, Academic Press, New York, 1964, Vol. 3.

17. Wilkins, M. L., "Calculation of Elastic-Plastic Flow," Univ. of Calif Lawrence Radiation Laboratory, Report 7322, 1963.

18. Courant. R. and D. Hilbert, *Methods of Mathematical Physics*, Interscience Publishers, New York, 1962, Vol. 2.

DOCUMENT CONTROL DATA · R&D
(Security classification of title, body of abstract and indexing annotation must be entered when the overall report is classified)

1. ORIGINATING ACTIVITY (Corporate author)	2a. REPORT SECURITY CLASSIFICATION
Stanford Research Institute 333 Ravenswood Avenue Menlo Park, California 94025	UNCLASSIFIED 2b. GROUP

3. REPORT TITLE

STRESS RELAXATION IN THE SHOCK COMPRESSION OF SOLIDS

4. DESCRIPTIVE NOTES (Type of report and inclusive dates)

6 December 1965-15 March 1967

5. AUTHOR(S) (Last name, first name, initial)

Anderson, Gordon D; Alverson, Roy C.; Murri, William J.;
Hanagud, Sathyanarayana V.

6. REPORT DATE	7a. TOTAL NO. OF PAGES	7b. NO. OF REFS
May 1967	116	18

8a. CONTRACT OR GRANT NO. AF 29(601)-7119	9a. ORIGINATOR'S REPORT NUMBER(S)
b. PROJECT NO. 5710	AFWL-TR-67-24
c. Subtask No. 15.018	9b. OTHER REPORT NO(S) (Any other numbers that may be assigned this report) Contractor's report number:
d.	SRI Project FGU-5783

10. AVAILABILITY/LIMITATION NOTICES This document is subject to special export controls and each transmittal to foreign governments or foreign nationals may be made only with prior approval of AFWL (WLRP), Kirtland AFB, NM, 87117. Distribution is limited because of the technology discussed in the report.

11. SUPPLEMENTARY NOTES	12. SPONSORING MILITARY ACTIVITY
	AFWL (WLRP) Kirtland AFB, NM 87117

13. ABSTRACT The purpose of the work reported here was to investigate nonsteady-state behavior in the early stages of one-dimensional shock propagation. This behavior has been termed stress relaxation. The work consisted of an experimental phase and a theoretical-computational phase. In the experimental phase, stress-time profiles resulting from impact by a gas-gun projectile were observed in hard and soft 2024 aluminum and in polyethylene at various distances from the plane of impact. Quartz gages were used for the measurements in aluminum, and manganin wire gages were used in polyethylene. Peak stress amplitudes were about 14 kbar in aluminum; there was a pronounced decay in amplitude of elastic precursor with propagation distance. The peak stress in polyethylene was varied from 3 to 11 kbar; nonsteady-state effects were also observed, although no elastic wave was evident. In the theoretical and computational phase, several mathematical models of stress relaxation were developed. Computations based on these models have been performed by the method of characteristics and by the artificial viscosity method of von Neumann and Richtmyer. It has been found that the two-parameter model of stress relaxation predicts the experimental results more closely than does the one-parameter model. During this investigation, it was found that no artificial viscosity is needed when stress-relaxing models are used. Some preliminary results on the inclusion of thermodynamic behavior have been obtained, and it is shown that a consistent model can be formulated on the basis of equilibrium thermodynamics.

(Distribution Limitation Statement No. 2)

DD FORM 1473
JAN 64

| 14. | LINK A | | LINK B | | LINK C | |
KEY WORDS	ROLE	WT	ROLE	WT	ROLE	WT
Shock propagation						
Stress relaxation						
Elastic-plastic						
Dynamic response						
Hugoniot						
Solid materials						
Metals						
Polymers						
Method of characteristics						
Artificial viscosity						

INSTRUCTIONS

1. ORIGINATING ACTIVITY: Enter the name and address of the contractor, subcontractor, grantee, Department of Defense activity or other organization (corporate author) issuing the report.

2a. REPORT SECURITY CLASSIFICATION: Enter the over-all security classification of the report. Indicate whether "Restricted Data" is included. Marking is to be in accordance with appropriate security regulations.

2b. GROUP: Automatic downgrading is specified in DoD Directive 5200.10 and Armed Forces Industrial Manual. Enter the group number. Also, when applicable, show that optional markings have been used for Group 3 and Group 4 as authorized.

3. REPORT TITLE: Enter the complete report title in all capital letters. Titles in all cases should be unclassified. If a meaningful title cannot be selected without classification, show title classification in all capitals in parenthesis immediately following the title.

4. DESCRIPTIVE NOTES: If appropriate, enter the type of report, e.g., interim, progress, summary, annual, or final. Give the inclusive dates when a specific reporting period is covered.

5. AUTHOR(S): Enter the name(s) of author(s) as shown on or in the report. Enter last name, first name, middle initial. If military, show rank and branch of service. The name of the principal author is an absolute minimum requirement.

6. REPORT DATE: Enter the date of the report as day, month, year; or month, year. If more than one date appears on the report, use date of publication.

7a. TOTAL NUMBER OF PAGES: The total page count should follow normal pagination procedures, i.e., enter the number of pages containing information.

7b. NUMBER OF REFERENCES Enter the total number of references cited in the report.

8a. CONTRACT OR GRANT NUMBER: If appropriate, enter the applicable number of the contract or grant under which the report was written.

8b, 8c, & 8d. PROJECT NUMBER: Enter the appropriate military department identification, such as project number, subproject number, system numbers, task number, etc.

9a. ORIGINATOR'S REPORT NUMBER(S): Enter the official report number by which the document will be identified and controlled by the originating activity. This number must be unique to this report.

9b. OTHER REPORT NUMBER(S): If the report has been assigned any other report numbers (either by the originator or by the sponsor), also enter this number(s).

10. AVAILABILITY/LIMITATION NOTICES: Enter any limitations on further dissemination of the report, other than those

imposed by security classification, using standard statements such as:

(1) "Qualified requesters may obtain copies of this report from DDC."

(2) "Foreign announcement and dissemination of this report by DDC is not authorized."

(3) "U. S. Government agencies may obtain copies of this report directly from DDC. Other qualified DDC users shall request through
_____ ."

(4) "U. S. military agencies may obtain copies of this report directly from DDC. Other qualified users shall request through
_____ ."

(5) "All distribution of this report is controlled. Qualified DDC users shall request through
_____ ."

If the report has been furnished to the Office of Technical Services, Department of Commerce, for sale to the public, indicate this fact and enter the price, if known.

11. SUPPLEMENTARY NOTES: Use for additional explanatory notes.

12. SPONSORING MILITARY ACTIVITY: Enter the name of the departmental project office or laboratory sponsoring (paying for) the research and development. Include address.

13. ABSTRACT: Enter an abstract giving a brief and factual summary of the document indicative of the report, even though it may also appear elsewhere in the body of the technical report. If additional space is required, a continuation sheet shall be attached.

It is highly desirable that the abstract of classified reports be unclassified. Each paragraph of the abstract shall end with an indication of the military security classification of the information in the paragraph, represented as (TS), (S), (C), or (U).

There is no limitation on the length of the abstract. However, the suggested length is from 150 to 225 words.

14. KEY WORDS: Key words are technically meaningful terms or short phrases that characterize a report and may be used as index entries for cataloging the report. Key words must be selected so that no security classification is required. Identifiers, such as equipment model designation, trade name, military project code name, geographic location, may be used as key words but will be followed by an indication of technical context. The assignment of links, rules, and weights is optional.

AIR FORCE WEAPONS LABORATORY
Air Force Systems Command
Kirtland Air Force Base
New Mexico 87117

8 January 1968

ERRATA

AFWL-TR-67-24   AIR TRANSPORTABILITY TESTING OF THE BTV UNIT IN THE
C-133 AIRCRAFT, November 1967

Cover: Change "AFWL" to "AFSWC" in three places.

C. W. HAIG
Chief, Reports and Data Branch
Technical Information Division